

A Review of Degradation Mechanisms and Recent Achievements for Na-Ion Layered Transition Metal Oxides

Jiameng Feng,^[a] De Fang,^[a] Jie Li,^[a] and Jianling Li^{*[a]}

Due to the low price and high specific capacity, sodium ion batteries (SIBs) have become a crucial candidate for the future large-scale energy storage power station, providing strong support for energy transition. Layered transition metal oxides (LTMOs), as one of the most promising cathode materials for SIBs, are usually accompanied by the sodiation/de-sodiation during charging/discharging, which leads to the slippage and deformation of the layered structure, and consequently causes to the degradation of electrochemical performance. The

degradation mechanisms of LTMOs attributed to the structural change are important references for improving the electrochemical performance of cathode materials. Here, this paper presents the main degradation mechanisms such as irreversible anion redox reaction, Na^+ /vacancy ordering transition and poor air stability as well as the corresponding modification means. It also summarizes the challenges faced by sodium-ion LTMOs cathode materials, and gives an outlook on the key issues that need to be solved for future development.

1. Introduction

The consumption of large amounts of fossil energy generates irreversible pollution and damage to the human environment. Therefore, there is an urgent need for an epoch-making energy revolution, replacing fossil energy with renewable energy to free humankind from the impending energy crisis and environmental disaster.^[1,2] In recent years, the technology of converting renewable energy sources (such as wind energy, solar energy and tidal energy) into electricity has been developing rapidly, but the generated electricity possesses the characteristics of randomness, intermittency and volatility. Consequently, it is necessary to develop the large-scale energy storage technology in order to significantly improve the effective availability of renewable energy,^[3,4] as well as establish a green, low-carbon and economical sustainable development-oriented society.^[5,6] In this context, sodium ion batteries (SIBs) are attracting attention in large-scale energy storage applications due to the abundant sodium resources.^[7,8]

Finding suitable cathode materials is the key to the practicality of SIBs. At present, the cathode materials for SIBs mainly include the transition metal oxides,^[9–11] polyanions,^[12–14] Prussian blue^[15–17] and organics.^[18] Among them, layered transition metal oxides (LTMOs) are one of the most commercially promising cathode materials for sodium-ion batteries because of their periodic layered structure, simple preparation method, as well as high specific capacity and voltage.^[19] LTMOs are the earliest studied class of embedded compounds, with the structural formula Na_xMO_2 (M is mainly one or more of the transition metal elements).^[20] Due to the large radius difference between sodium ions (1.02 Å) and transition metal ions, sodium ions are easier to separate from the transition metal ions to

form a layered structure at high temperatures, which makes the stacking mode of Na-ion LTMOs diversified. Usually, the MO_6 octahedral structure formed by transition metal elements and the surrounding six oxygens constitutes a transition metal (TM) layer, and sodium ions are located between the TM layers, forming a layered structure alternating between the MO_6 polyhedral layer and the NaO_6 (AM) layer. Delmas et al.^[21] classifies LTMOs into different structures (such as O3, O2, P3 and P2) according to the ligand configuration of the sodium ions in the MO_6 polyhedra and the stacking method of the oxygen. The capital letters represent the coordination configuration of the sodium ions and the numbers represent the number of stacking layers of the least repetitive unit of oxygen. The structure of LTMOs cathode materials is customisable through appropriate component modulation and process conditions. In recent years, researchers have achieved a great improvement in the electrochemical performance of cathode materials by modulating reasonable transition metal components,^[22,23] constructing heterogeneous structures,^[24] and coating stable surfaces.^[25] However, as shown in Figure 1, the Na^+ /vacancy ordering transition, irreversible phase transition, irreversible anionic redox and transition metal dissolution have adverse effects on the structural stability, voltage platform, sodium ion diffusion rate and other characteristics of SIBs, thus affecting the overall electrochemical performance of cathode materials for SIBs.^[26,27] LTMOs are promising cathode materials for sodium ion batteries^[28–30] and the basic scientific problems and modification strategies of LTMOs are introduced in the following.

2. Anionic redox reaction

Currently, sodium-ion batteries are in urgent need of high-capacity and long-life cathode materials for the applications in large-scale energy storage. The charge compensation of conventional cathode materials for SIBs is based on the redox

[a] Dr. J. Feng, M.Sc. D. Fang, M.Sc. J. Li, Prof. J. Li

State Key Laboratory of Advanced Metallurgy, University of Science and Technology Beijing, Beijing 100083, China
E-mail: lijianling@ustb.edu.cn

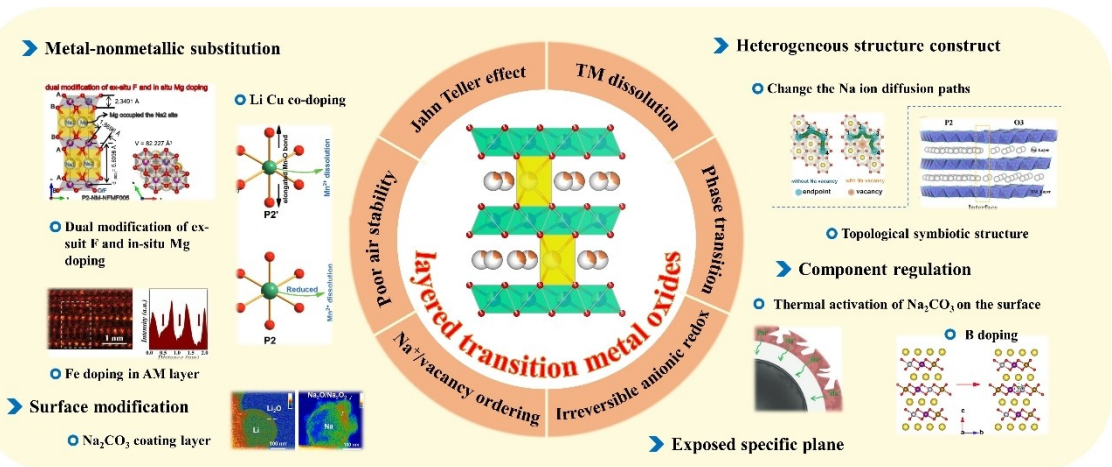


Figure 1. Current challenges arising in layered transition metal oxides for SIBs and emerging solutions.^[31–37]

reaction of transition metal ions, such that the energy density of the cathode materials is mainly limited by the content of metastable transition metal ions.^[38,39] In addition to transition metal ions, anionic redox reactions can be stimulated during sodium ion de-embedding by substituting Li⁺ or Mg²⁺ for transition metal ions in the Na_xTMO₂, resulting in high capacity and high voltage.

2.1. Anionic redox mechanism

The Li-rich manganese-based materials (such as Li₂MnO₃) show additional capacity beyond the theoretical capacity, and the extra capacity is provided by lattice oxygen in the bulk phase. Expanding and analyzing the structure of Li₂MnO₃, Li and Mn alternately occupy different octahedral positions, which leads to an O3-type structure with a hexagonal crystal system. In the



Jiameng Feng is currently pursuing her PhD at the University of Science and Technology Beijing. Her research interests mainly focus on the synthesis of cathode materials for sodium-ion and lithium-ion batteries, as well as the relation between microstructures and electrochemical performance of cathode materials.



Jianling Li is the Professor at the University of Science and Technology Beijing. She received PhD degree from the Harbin Institute of Technology in 1998. She then joined the Tsinghua University as a postdoctoral researcher from 1999 to 2001. Since 2001, she has been a professor at the University of Science and Technology Beijing. She was an academic visitor at Aichi Institute of Technology in 2003–2004. Her research focuses on lithium/sodium ion batteries electrode material, supercapacitor, solid-state batteries and new electrochemical energy storage technology.



De Fang graduated from the University of Science and Technology Beijing in 2022 with bachelor's degree and joined Professor Jianling Li's research group at University of Science and Technology Beijing in the same year. His current research is on high performance layered oxide cathode materials for sodium ion batteries, especially terms of their excellent cycling and structure stability.



Jie Li graduated from the University of Science and Technology Beijing in 2023 with bachelor's degree. He is currently pursuing his M.Sc. degree at the University of Science and Technology Beijing. His current research is on high performance layered oxide cathode materials for sodium ion batteries.

same oxygen skeleton structure, the excess Li will partially replace Mn, transforming it into a monoclinic structure. The excess Li penetrates into the TM layer and the characteristic peaks of the monoclinic structure are between 20° and 30°. It is the difference in charge and size between Li^+ and Mn^{4+} that leads to the formation of the honeycomb arrangement structure of LiMn_6 . For LTOs with Li/TM superlattice structure, the oxide ions are coordinated by three TM ions and three Li

ions, as shown in Figure 2a. Since the Fermi energy levels are located in orbitals with TM, the capacity of LiTMO_2 originates from cationic redox (Figure 2b). In Li-rich cathode materials, the oxide ions are coordinated by two TM ions and four Li ions in $\text{Li}-\text{O}-\text{Li}$ configuration (Figure 2c), which is due to Li occupying the TM sites. Because there is a large energy difference between Li 2s orbitals and O 2p orbitals, the hybridization is limited, resulting in the formation of non-bonded O 2p orbitals, which

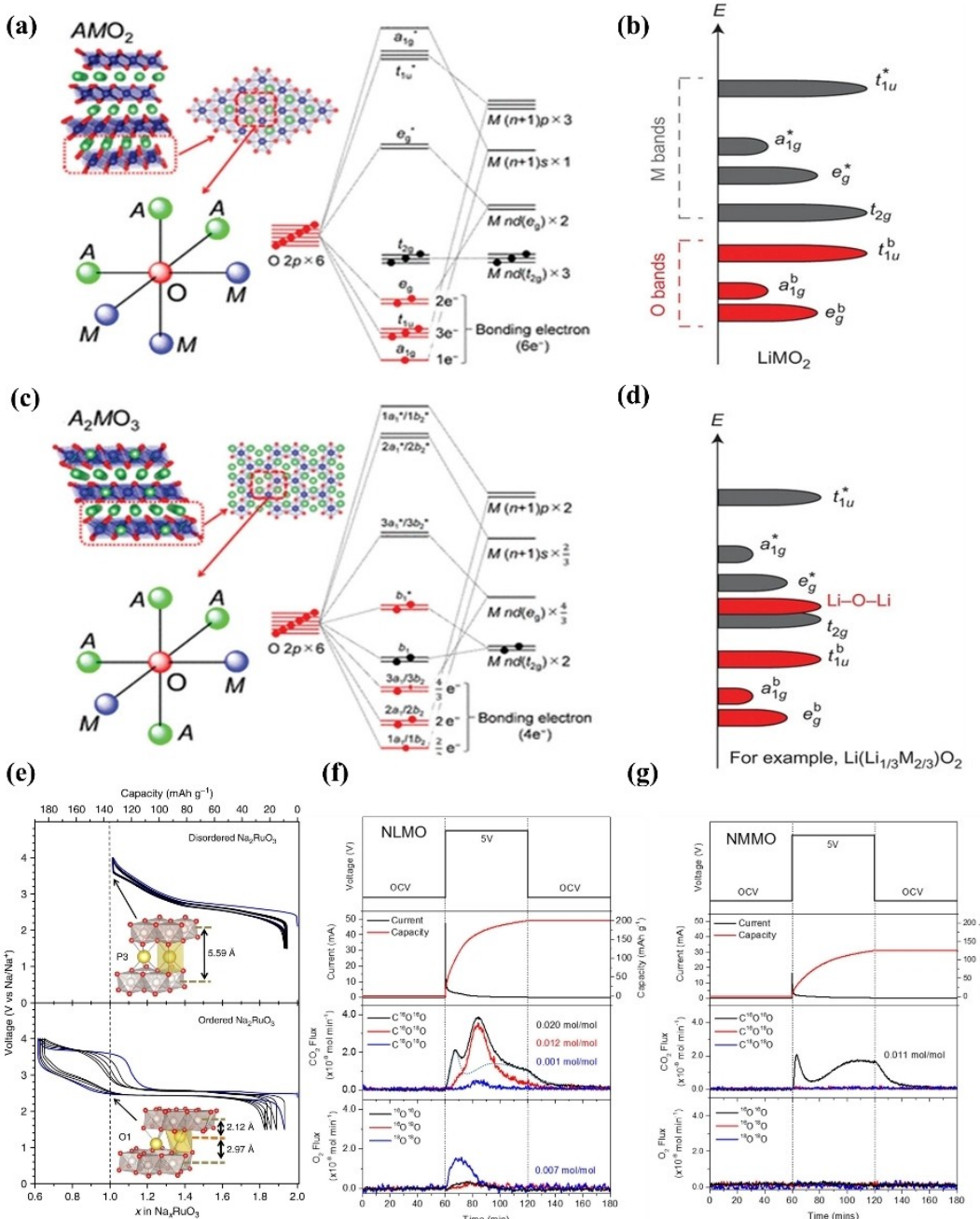


Figure 2. Schematic illustration of the local arrangement around oxygen, and the corresponding molecular orbital of (a) stoichiometric AMO_2 and (c) alkali-ion excess A_2MO_3 . The band structure of (b) stoichiometric layered oxide and (d) Li-excess layered oxide with $\text{Li}-\text{O}-\text{Li}$ configurations.^[40] Copyright 2023 Wiley-VCH GmbH. (e) Galvanostatic cycling curves record at 30 mAh g⁻¹ for disordered and ordered Na_xRuO_3 with the first cycle highlighted in blue. Insets show the coordination environment of Na at $x=1.0$ for each phase.^[47] Copyright 2016 The Author(s). OEMS of ¹⁸O-labeled (f) NLMO versus (g) NMNO subjected to a potential step of 5 V for a period of 1 h. The top panel shows the potential profile, the middle panel shows the current and capacity response and the bottom panel shows the traces from operando mass spectrometry.^[49] Copyright 2022 American Chemical Society.

allows for the removal of electrons from the non-bonded O 2p (Figure 2d), that is, the anionic redox.^[40]

The non-bonded O 2p is the second energy band besides the anti-bonded state (M–O)* energy level that can provide charge compensation while maintaining the structural stability. Through the above series of presentations, it can be found that the introduction of oxygen redox reaction in oxide-based cathode materials is a strategy that can effectively enhance the capacity of SIBs. However, the oxygen redox reaction is usually accompanied by the evolution of long-range and local structures in the LTMOs, such as O–O dimer formation and lattice oxygen precipitation. These irreversible structural evolutions will cause anisotropic lattice strains and huge cell volume changes in the cathode materials, which will lead to rapid degradation of battery performance.^[41] As a result, how to solve the problem of mutual constraints between capacity and structural stability, breaking through this constraint as well as achieving high capacity and high stability at the same time, is a major challenge in the research of cathode materials for SIBs.

2.2. Anionic redox in different configurations

In the early studies, the anionic redox reactions of LTMOs for sodium ion batteries were limited to Na-rich materials containing the Na-TM–O configuration. As research progressed, more and more materials with anionic redox reactions were discovered.^[42–44] In addition to alkali metals, alkaline earth metals (AE), vacancies (\square), and some transition metals (TM) also can stimulate anionic redox reactions in cathode materials.^[33,45,46]

2.2.1. The Na-TM–O configuration

Yamada et al.^[47] report two kinds of ordered and disordered Na_2RuO_3 cathode materials by controlling the synthesis conditions, both of which belong to the $\bar{R}\bar{3}m$ space group but have different atomic arrangements and electrochemical performance. In the disordered Na_2RuO_3 , Na and Ru show a disordered arrangement in the TM layer, thus calling it disordered phase. In the ordered Na_2RuO_3 , Na and Ru show an ordered honeycomb arrangement in the TM layer, which is similar to the structure of Li_2MnO_3 . By comparison, it is found that the two cathode materials with different configurations possess different electrochemical performance. As shown in Figure 2e, the ordered phase Na_2RuO_3 shows a specific capacity of 180 mAh g^{-1} in the voltage range of 1.5–4.0 V, which corresponds to the 1.3 Na^+ de-embedding. And its charging curves present a step-like pattern, with plateaus at 2.5 V and 3.6 V, which corresponds to $\text{Ru}^{4+}/\text{Ru}^{5+}$ and $\text{O}^{2-}/(\text{O}_2)^{n-}$ redox. In contrast, there is only the $\text{Ru}^{4+}/\text{Ru}^{5+}$ to provide charge compensation during charging/discharging for the disordered Na_2RuO_3 , with no anionic redox reactions to provide capacity. In addition to Ru, the Na_2IrO_3 also possesses anionic redox activity. Coincidentally, the Na_2IrO_3 possesses two different configurations, a transition-metal disordered layered structure and a transition-metal ordered

layered structure, which show large differences in electrochemical performance.^[48]

2.2.2. The Na-Li (Mg)-O configuration

When the transition metal ions in the TM layer are replaced by the alkali metal Li, a Na–O–Li configuration is created in the cathode materials.^[50,51] Huang et al.^[52] report the P3- $\text{Na}_{0.6}\text{Li}_{0.2}\text{Mn}_{0.8}\text{O}_2$ with an anionic redox reaction, where Li replaces some of the Mn to occupy the TM layer. The P3- $\text{Na}_{0.6}\text{Li}_{0.2}\text{Mn}_{0.8}\text{O}_2$ shows a charging specific capacity of 100 mAh g^{-1} and a discharge specific capacity of 75 mAh g^{-1} at the current density of 30 mA g^{-1} in the high voltage range of 3.5–4.5 V. The capacity retention rate is 49.3% after 30 cycles. X-ray photoelectron spectroscopy (XPS) and X-ray absorption near edge structure (XANES) prove that the oxygen directly participates in the charge compensation during charging, and that the $\text{O}^{2-}/(\text{O}_2)^{n-}$ redox reaction provides capacity to the cathode material. Alike cathode materials for SIBs are P2- $\text{Na}_{5/6}\text{Li}_{1/4}\text{Mn}_{3/4}\text{O}_2$,^[53] P2- $\text{Na}_{0.6}[\text{Li}_{0.2}\text{Mn}_{0.8}]\text{O}_2$,^[54] and P2- $\text{Na}_{0.72}\text{Li}_{0.24}\text{Mn}_{0.76}\text{O}_2$.^[55] Similar to Li-rich materials, the anionic redox activity of these materials benefits from the non-bonded O 2p, and the oxygen redox reaction significantly increases the specific capacity of the cathode materials. However, the higher charging voltage causes to the generation of peroxygen-like groups, side reactions, and thus irreversible oxygen loss, which ultimately leads to severe long-cycle capacity degradation and affects the battery life. In addition to Li, researchers find that Mg^{2+} also exhibits reversible anionic redox characteristics, and the shape of the charge/discharge curves is similar to that of Na–Li–Mn–O, showing a more robust structure and electrochemical stability. Burce et al.^[49] explore the causes of oxygen deficiency during long cycling in the LTMOs with anionic redox reactions by comparing P2- $\text{Na}_{0.67}\text{Mg}_{0.28}\text{Mn}_{0.72}\text{O}_2$ (NMMO) and P2- $\text{Na}_{0.78}\text{Li}_{0.25}\text{Mn}_{0.75}\text{O}_2$ (NLMO). At the high voltage, both Na^+ and Li^+ are de-embedded from NLMO, leading to non-bonded oxygen (less than 3 cationic ligand oxygen) and surface-localised oxygen deficiency (Figure 2f). In contrast, the oxygen is coordinated with at least two Mn^{4+} and one Mg^{2+} for NMMO, which stabilizes the oxygen and avoids oxygen deficiency (Figure 2g). The authors demonstrate that oxygen deficiency is not a result of the redox it undergoes or of the detachment of excess alkali metal ions from the TM layer, but is triggered in a state of severe embedded bonding of cations when there is nearly depleted alkali metal ion for cathode materials. Therefore, strategies such as stabilizing non-bonded oxygen in the near-surface region of the cathode material particles to avoid oxygen deficiency are important methods to increase the battery capacity and improve the life, such as $\text{Na}_{0.71}\text{Li}_{0.22}\text{Al}_{0.05}\text{Mn}_{0.73}\text{O}_2$,^[56] P2- $\text{Na}_{0.7}\text{Li}_{0.03}[\text{Mg}_{0.15}\text{Li}_{0.07}\text{Mn}_{0.75}]\text{O}_2$,^[57] and $\text{Na}_{0.67}\text{Fe}_{0.5}\text{Mn}_{0.45}\text{Ru}_{0.05}\text{O}_2$.^[58]

2.2.3. The Na- \square -O configuration

Vacancies in transition metal layered oxide cathode materials can also stimulate anionic redox reactions. Yamada et al.^[59] investigate anionic redox of $\text{Na}_2\text{Mn}_3\text{O}_7$, a cathode material that can be written as $\text{Na}_{4/7}(\square_{1/7}\text{Mn}^{4+})_{6/7}\text{O}_2$, with a certain amount of Mn vacancies in the transition metal layer. Here, Mn^{4+} is difficult to be oxidised, but $\text{Na}_2\text{Mn}_3\text{O}_7$ shows a specific capacity of 75 mAh g^{-1} at a voltage range of 3.0 to 4.7 V and a specific capacity of 200 mAh g^{-1} at a voltage range of 1.5 to 4.7 V. As shown in the XANES tests of Figure 3a, the Mn-L edge does not significantly change during charging/discharging, indicating that Mn is not involved in the redox. By contrast, the O-K edge increases in the edge front area, which illustrates the redox of $\text{O}^{2-}/(\text{O}_2)^{n-}$ in the $\text{Na}_2\text{Mn}_3\text{O}_7$ (Figure 3b,c). The vacancies in the transition metal layer of P2- $\text{Na}_{0.7}\text{Mg}_{0.2}[\text{Fe}_{0.2}\text{Mn}_{0.6}\square_{0.2}]\text{O}_2$ form the “ $\square\text{-O-}\square$ ”, “ $\text{Na-O-}\square$ ” and “ $\text{Mg-O-}\square$ ” configurations, triggering oxygen redox reactions during charging/discharging.^[60] From the XANES in Figure 4a-f, the valence state of Mn changes from +3.8 to +4, providing a capacity of 33.1 mAh g^{-1} . The valence state of Fe changes from +3 to +3.5, providing a capacity of 27.6 mAh g^{-1} . All of these suggest that the extra capacity is provided by anions, and a portion of O^{2-} is oxidised to O^- as shown in Figure 4g-i. DFT calculations show that it is the oxygen around the vacancies that contributes to the charge compensation, similar to the “Li-O-Li” configuration in lithium-ion batteries. A novel P2- $\text{Na}_{0.76}\text{Ca}_{0.05}[\text{Ni}_{0.23}\square_{0.08}\text{Mn}_{0.69}]\text{O}_2$ cathode material is designed by Qu et al.^[46] The vacancies located in the transition metal layer are able to form “ $\text{Na-O-}\square$ ” and “ $\square\text{-O-}\square$ ” configurations, which generate non-bonded O 2p orbitals, thus effectively stimulating the oxygen valence change.

3. Na^+ /vacancy ordering

3.1. Formation of Na^+ /vacancy ordering

There is often an ordered distribution of Na^+ /vacancy in the TM layer for LMOs, which occurs in O3-type,^[61,62] P2-type,^[63,64] and

P3-type^[65] cathode materials, essentially resulting in the formation of new superlattice phases and manifesting as a step-like voltage drop on charge/discharge curves. Sodium ions are subjected to the electrostatic interaction of the surrounding Na–Na, Na–O, and Na-TM, and spontaneously sort in the AM layer following the principle of lowest energy during charging/discharging. The metastable phases generate during de-embedding of Na^+ due to the re-arrangement of different Na^+ /vacancy ordering, and the sodium ions need to overcome additional energy barriers for de-embedding, which results in a stepped voltage plateau on the charge-discharge curves. The Na^+ /vacancy ordering usually corresponds to a few specific sodium contents: 1/3, 1/2, 5/8, and 2/3. For example, P2- Na_xCoO_2 shows a charge-discharge curve with a total of 9 voltage plateaus (Figure 5a) due to the Na^+ /vacancy ordering transition, each of which separates the solid-solution curve into two segments.^[66] Similarly, the Na^+ /vacancy ordering transition is observed at $x=1/2$ for P2- Na_xVO_2 , and the X-ray diffraction (XRD) spectrum shows specific superlattice peaks.^[67] It has been shown in a number of studies that the Na^+ /vacancy ordering transition hinders the migration of sodium ions within the layer, which adversely affects the performance of sodium-ion batteries.^[68-70]

3.2. Exploit disordered Na^+ /vacancy

Currently, in order to make the Na^+ /vacancy disordering, different kinds of cation doping are mainly used to inhibit ordering in the sodium layer or to construct disordered Na^+ /vacancy, eliminate the step-voltage platform to improve the sodium ion transport kinetics and enhance the electrochemical performance of the materials.

3.2.1. Disturb Na^+ /vacancy ordering by single element doping

Guo et al.^[71] design a P2- $\text{Na}_{2/3}\text{Ni}_{1/3}\text{Mn}_{1/3}\text{Ti}_{1/3}\text{O}_2$ (P2-NaNMT) cathode material with completely disordered Na^+ /vacancy by

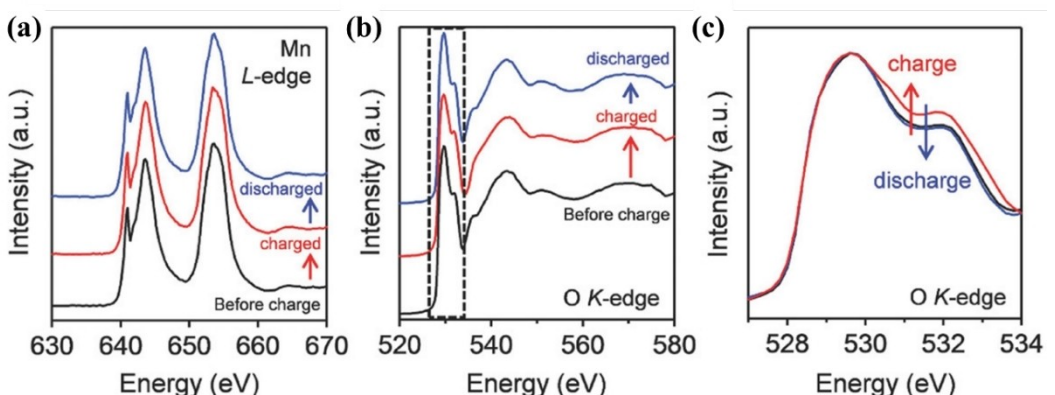


Figure 3. Electronic structure changes of $\text{Na}_2\text{Mn}_3\text{O}_7$ during the charge and discharge: (a) Ex situ X-ray absorption spectra for Mn L_3 -edge; (b) Ex situ X-ray absorption spectra for O K-edge; (c) Enlarged part of X-ray absorption spectra for O K-edge.^[59] Copyright 2018, Wiley-VCH Verlag GmbH & Co. KGaA.

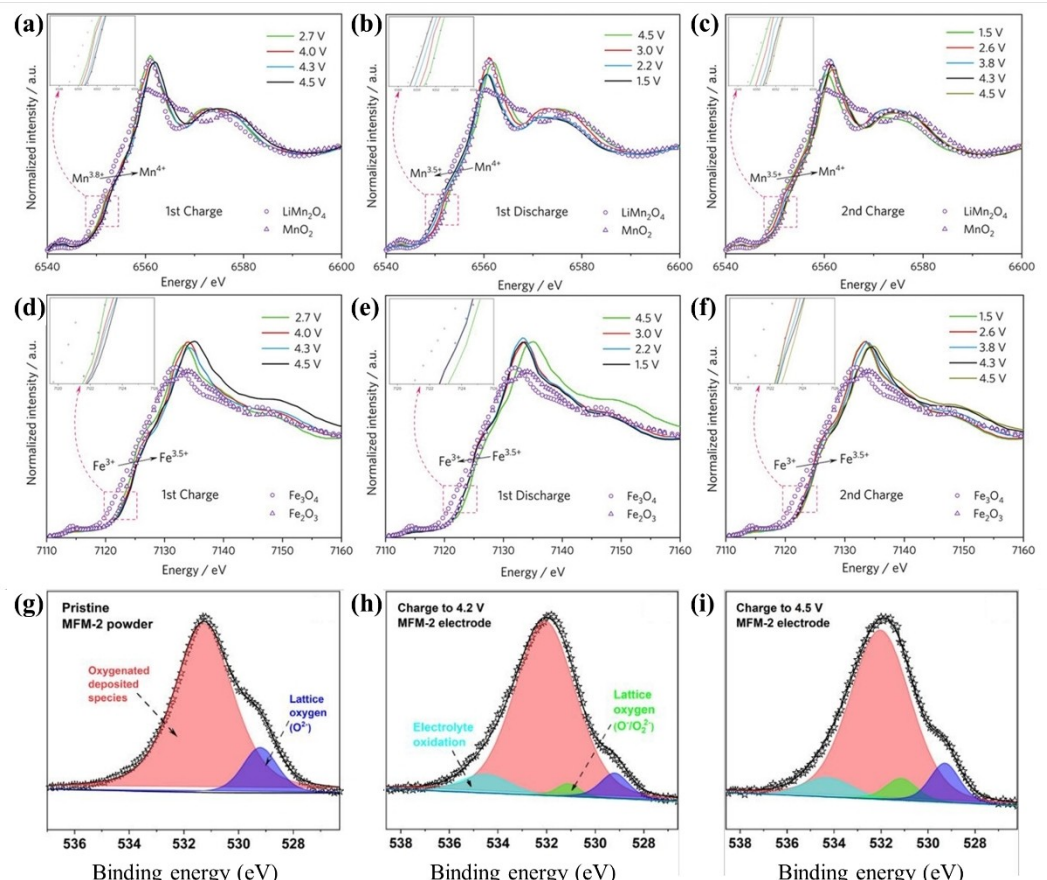


Figure 4. Charge compensation mechanism of MFM-2 during cycling. (a–c) Mn and (d–f) Fe K-edge XANES of MFM-2 at various states in the first cycle and second charge state. XPS spectrums of O 1s for MFM-2 at different states: (g) pristine powder; (h) electrode charged to 4.2 V; (i) electrode charged to 4.5 V.^[60] 2021 Wiley-VCH GmbH.

introducing Ti into P2-Na_{2/3}Ni_{1/3}Mn_{2/3}O₂. It is shown that the disordered Na⁺/vacancy eliminates the voltage plateau due to the ordered re-arrangement of Na⁺/vacancy, and the whole electrochemical process is completely a ramp-type solid-solution reaction (Figure 5b,c), which dramatically improves the electrochemical performance of the P2-type cathode material at higher current density (Figure 5d). First-principles density functional theory (DFT) calculations (Figure 5e,f) show that the Ti doping narrows the site-energy difference between Na_e and Na_f, which significantly improves the diffusion properties of sodium ions between the TM layers. Wang et al.^[73] effectively suppress the Na⁺/vacancy ordering transition by Li doping, and the cathode material P2-Na_{0.85}Li_{0.12}Ni_{0.22}Mn_{0.66}O₂ undergoes complete solid solution reaction during charging/discharging. There is no voltage plateau in the charge-discharge curves, so the structure is well stabilized, as well as the rate performance and long-cycling performance of the battery are improved. Zhou et al.^[72] modulate the ratio of Na_e/Na_f by introducing Sb⁵⁺ with high valence, which creates strong repulsive force on Na_f below or above Sb⁵⁺, causing Na_f move to the Na_e site (Figure 5g). The novel P2-Na_{0.67}[Mn_{0.61}Ni_{0.28}Sb_{0.11}]O₂ cathode material reduces the ratio of Na_f/Na_e from 0.63 to 0.44, and improves the electrochemical performance of sodium storage materials. Zhao et al.^[74] design Na_{0.67}Ni_{0.3}Co_{0.1}Mn_{0.6}O_{1.94}(BO₃)_{0.02} as an cathode

material for sodium-ion batteries by accurately doping B into the lattice of the P2-phase material based on DFT calculations. It is energetically favourable to enter into the oxygen layer to form a unique BO₃ configuration. The BO₃ conformation can better support the P2 structure, and at the same time will generate electrostatic repulsion to the surrounding Na, repelling the Na occupying the Na_f site to Na_e occupancy, thus effectively inhibiting the Na⁺/vacancy ordering transition and significantly improving the electrochemical performance. In summary, it is necessary to further construct the disordered Na⁺/vacancy structure to eliminate the stepped voltage plateau, enhance the structural stability, and improve the kinetics of sodium ion transport.

3.2.2. Disturb Na⁺/vacancy ordering by multielement doping

Zhang et al.^[75] effectively suppress the Na⁺/vacancy ordering transition by double-ion (Cu²⁺ and Zn²⁺) doping, and the diffraction peaks at 27.2° and 28.4°, representing Na⁺/vacancy ordering, disappear from the XRD pattern of the double-doped cathode material. Xiao et al.^[76] introduce Li and Ti into P2-Na_{2/3}Ni_{1/3}Mn_{2/3}O₂, and the Li⁺ helps to increase the content of sodium ions in the AM layer, as well as Ti⁴⁺ can help to break

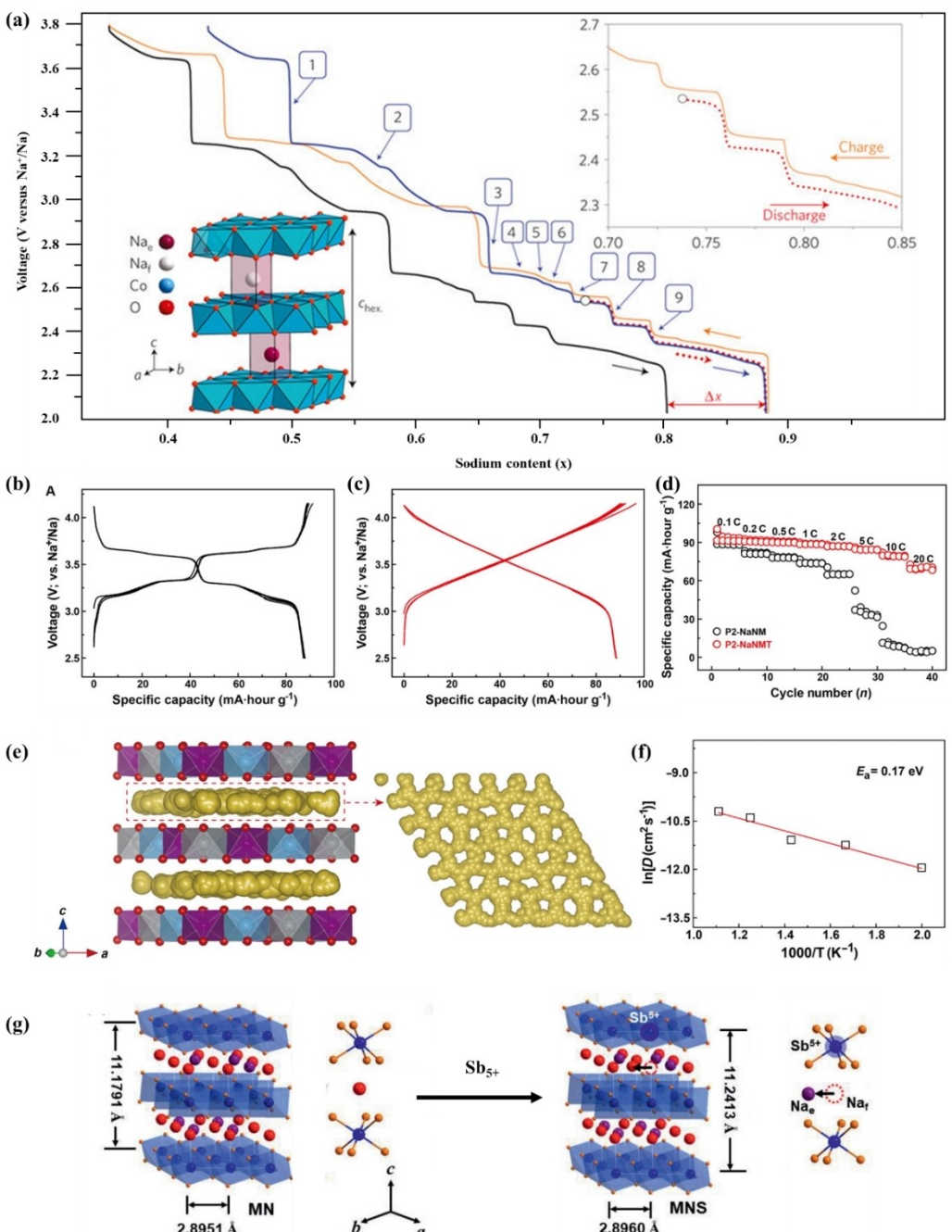


Figure 5. (a) The galvanostatic cycling curves of a Na//P2– $\text{Na}_0.5\text{CoO}_2$ battery.^[66] Copyright 2010, The Authors. Typical charge/discharge profiles of (b) P2-NaNM and (c) P2-NaNM-T between 2.5 and 4.15 V at a rate of 0.1 C. (d) The rate performance comparison of P2-NaNM and P2-NaNM-T samples at different rates. (e) Trajectories of Na^+ in P2-Na_{0.5}NMT simulate at a temperature of 800 K. The top view of each Na^+ layer is given in the right panel. (f) Arrhenius plot of Na^+ diffusion coefficients.^[71] Copyright 2018, The Authors. (g) The schematic of structure change from P2-MN to P2-MNS caused by Sb substitution.^[72] Copyright 2021, Wiley-VCH GmbH.

the Na^+ /vacancy ordering arrangement and create conditions for Na^+ remapping. The Na^+ /vacancy ordering of the AM layer in the material is successfully disturbed and more sodium ions tend to occupy the Na_e sites (Figure 6). The modified material exhibits excellent kinetic performance. The computational results show that the disordered AM layer arrangement and the preferential occupation of Na_e sites provide a good coordination environment for the transport for sodium ions.

4. Air stability

4.1. Effect of poor air stability on cathode materials

Air-sensitive electrode materials can deteriorate by reacting with H_2O and CO_2 in the air. When using the method of squeegee coated slurry to prepare cathode sheets for SIBs, it is often found that the slurry is sticky and possesses poor

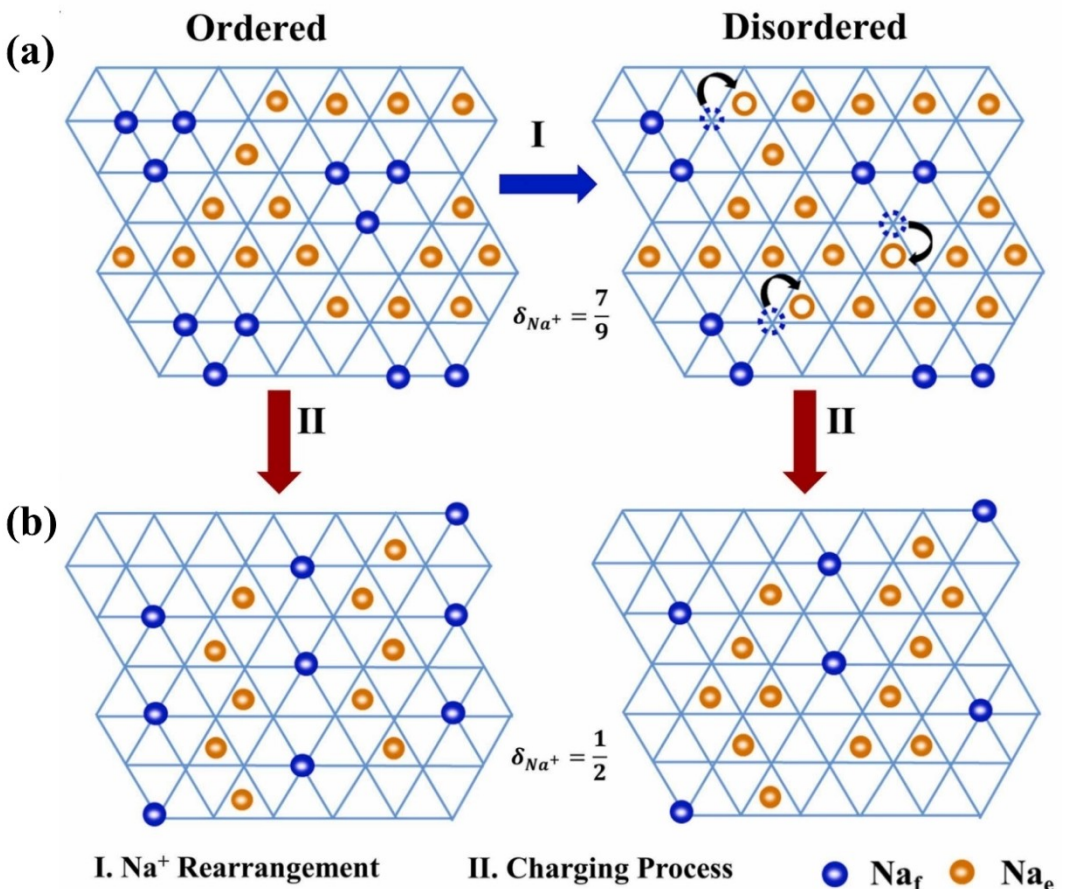


Figure 6. (a) Schematic diagram of the process of Na^+ rearrangement. (b) Schematic diagram of the Na^+ distribution change with ordered and disordered Na^+ /vacancy arrangements upon a certain amount of Na^+ extraction.^[75] Copyright 2022, Elsevier.

adhesion. For example, $\text{NaNi}_{0.5}\text{Mn}_{0.5}\text{O}_2$, conductive carbon and binder solution are mixed in air to make slurry and coat on the aluminum foil. The obtained the cathode sheet shows particle agglomeration and surface roughness phenomenon because of the strong alkaline of $\text{NaNi}_{0.5}\text{Mn}_{0.5}\text{O}_2$ particles. The OH^- will react with polyvinylidene difluoride (PVDF) in the slurry, which causes the F^- take off from the PVDF and the PVDF become poor adhesion. Besides, aluminium foil will react with OH^- (corrosion of aluminium foil), leading to electrochemical performance degradation or even failure for SIBs. Worse still, most of LTMOs for SIBs will react with moist air to form impurities (NaOH , Na_2CO_3) on the particle surface, which will lead to a series of side reactions during charging and discharging, and the battery's Coulombic efficiency and cycle life will be greatly reduced.^[77] Therefore, this kind of material should pay extra attention to the drying treatment of air in the process of preservation and preparation of pole pieces, which also raises the storage and transport cost for sodium-ion batteries cathode materials.^[78]

4.2. Factors affecting the air stability

The air stability of a material is closely related to its structure, elemental composition and morphology.^[79] In terms of material structure, the air stability of the material with a layered structure is weaker than that of the material with a tunnel-type structure, which can be found in the comparison between $\text{Na}_{0.44}\text{MnO}_2$ and $\text{Na}_{0.67}\text{MnO}_2$. The typical tunnel-type oxide $\text{Na}_{0.44}\text{MnO}_2$ possesses a unique S channel (Figure 7a), which ensures structural stability during cycling and is very stable in both air and water, but its specific discharge capacity is low,^[80,81] as show in Figure 7b,c. In contrast, $\text{Na}_{0.67}\text{MnO}_2$ possesses a high specific discharge capacity, but it is easy to react with H_2O and CO_2 in the air to generate surface impurities, resulting in layered structure instability and electrochemical performance decline.^[82–84] In terms of elemental composition, it is the stronger alkalinity of sodium ion that leads to a weaker air stability for sodium ion electrode materials compared to lithium ion electrode materials. Compared with LiOH , NaOH is highly hydrophilic and can absorb large amounts of water.^[85] In terms of morphology, materials with high specific surface area are more likely to absorb water and cause metamorphic reactions, so air sensitivity is also higher. In general, materials with hollow structures or nanoforms possess a large specific surface area,

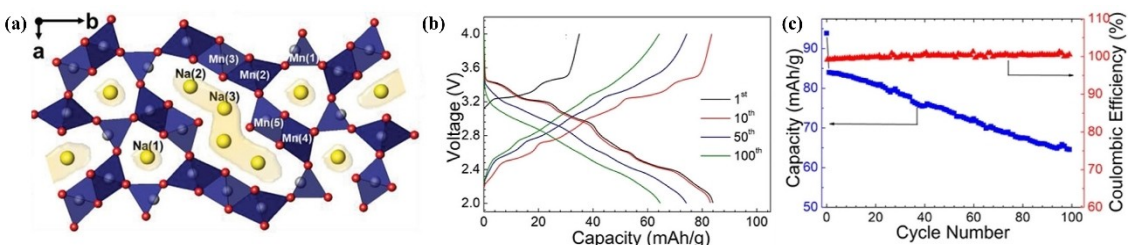


Figure 7. (a) The structural diagram of tunnel type oxides.^[9] Copyright 2020, WILEY-VCH Verlag GmbH & Co. KGaA, Weinheim. (b) The charge/discharge curves of Na_{0.44}MnO₂. (c) The charge/discharge curves of Na_{0.44}MnO₂.^[81] Copyright 2023, The Authors. Published by American Chemical Society.

high surface energy, and abundant surface/structural defects, which may be hygroscopic or more inclined to react with air molecules.^[86]

4.3. Tactics of enhancing the air stability

Based on these, researchers work to enhance the air stability to obtain LTMos cathode materials with excellent performance. By doping small amounts of cationic or anionic atoms into the lattice of sodium ion batteries cathode materials, the air/water stability can be significantly improved.^[82,88] This generally includes cationic dopants (Al, Mg, Ca, Ti, Nb, and B) and anionic dopants (F, Cl, and S). Among the above dopants, Al, Mg and Fe are considered to be the most promising elements due to their low cost. In addition, constructing a surface coating layer is one of the most important and effective strategies to improve the air stability of cathode materials. The purpose is to isolate H₂O and CO₂ from the air, avoid the formation of residual sodium compounds on the surface, and improve the air/water stability. At the same time, the surface coating layer can also act as a physical barrier to prevent the direct contact between the cathode materials and the organic electrolyte as well as inhibit the side reactions, thus improving the cycle life, safety performance and energy density of SIBs. Typically, the materials used to build a protective layer on the surface of cathode materials include metal oxides (ZrO₂,^[89] SnO₂,^[90] Al₂O₃,^[91] MgO,^[92] ZnO^[89]), phosphates ((NH₄)₂HPO₄, AlPO₄), fluorides (MgF₂,^[93] LiF^[94]), fast ionic conductors (Na₃PO₄^[95]), and organic cladding layers.^[96-98]

4.3.1. Elements doping

Sodium layered oxides show worse air stability than lithium layered oxides. On the one hand, stronger alkalinity of Na⁺ causes the Na⁺/H⁺ exchange reaction to carry out thoroughly. On the other hand, the sodium layer spacing is larger due to the large radius of Na⁺, coupled with a large number of vacancies, easily leading to the insertion of H₂O. What's worse, the NaOH formed on the surface possesses a strong hygroscopic property, which will quickly absorb a lot of H₂O and accelerate the Na⁺/H⁺ exchange reaction. Further, NaOH reacts with CO₂ in the air to form Na₂CO₃, which eventually forms a very thick alkaline insulation layer on the surface of materials. The specific capacity of materials will be greatly reduced during

the de-sodiation because of the Na⁺/H⁺ exchange reaction. The existence of alkaline insulation layer on the surface will increase the impedance. The H⁺ or H₂O inside the structure will hinder the Na⁺ transition, resulting in a decline in the rate performance.

Elements doping can reduce the formation of surface impurities and improve the air stability of the material by inhibiting H₂O embedding into the layered structure. There are three main theories for enhancing air stability through doping. Firstly, the interlayer occupancy R_n (the ratio of the volume of sodium ions to the overall volume of sodium layers) of sodium ions is increased by doping, thereby inhibiting Na⁺ removal and H₂O embedding. Li et al.^[99] increase the interlayer occupancy of sodium ions by Fe doping, drastically reducing the surface impurities of the layered oxides, as well as enhancing the air stability and electrochemical performance. The XPS in Figure 8 shows that the C and O contents on the surface of the cathode material are reduced. Na_{0.80}Li_{0.13}Ni_{0.20}Fe_{0.1}Mn_{0.57}O₂ exhibits an enhanced Coulombic efficiency during the first cycle, which suggests that the reduction of the surface impurities also reduces the side reactions at the electrode-electrolyte interface. Secondly, increasing the redox voltage of cathode materials can effectively prevent Na⁺/H⁺ exchange, thereby reducing surface impurities and improving the air stability of cathode materials. Komaba et al.^[100] prepare the O₃-Na_{5/6}Fe_{1/3}Mn_{1/2}Cu_{1/6}O₂ and O₃-Na_{5/6}Fe_{1/3}Mn_{1/2}Mg_{1/6}O₂ by Cu(Mg) doping, and Cu or Mg can improve the redox voltage of cathode materials. The exposed Cu(Mg)-doped cathode materials are well crystallized, and there is no impurity peak. In contrast, there are many diffraction peaks of the hydrated phase in the exposed O₃-Na_{5/6}Fe_{1/2}Mn_{1/2}O₂. Cu(Mg) doping can effectively prevent Na⁺/H⁺ exchange, which reduces the surface impurities and improves the air stability of the cathode materials. Yu et al.^[101] report that Na_{0.98}Ca_{0.01}[Ni_{0.5}Mn_{0.5}]O₂ shows improved cycling, thermal and air stability by 1 at% Ca doping. Thirdly, the superlattice ordering of TM atoms in the transition metal layer is beneficial to improve air stability.^[102,103] Lu et al.^[104] identify that H₂O cannot be inserted into P2-Na_{2/3}[Ni_{1/3}Mn_{2/3}]O₂ and attribute this advantage to the superlattice ordering of Ni and Mn atoms in the transition metal layers. The special superlattice ordering induces strong interlayer interactions between adjacent transition metal layers and inhibits H₂O absorption.

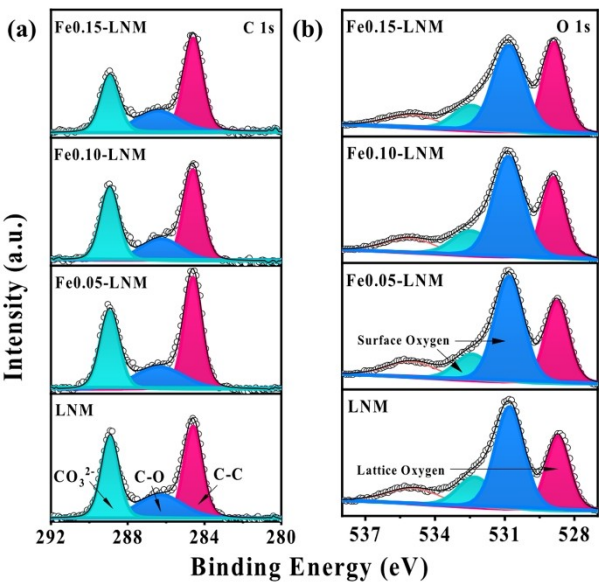


Figure 8. The XPS spectroscopy of (a) C 1s and (b) O 1s in different samples.^[99] Copyright 2022 Elsevier B.V.

4.3.2. Construct surface coating layer

Sivakumar et al.^[90] construct a SnO coating layer on the surface of $\text{Na}_{0.4}(\text{Mn}_{0.33}\text{Co}_{0.33}\text{Ni}_{0.33})\text{O}_2$ by liquid-phase precipitation, which prevents the destruction of $\text{Na}_{0.4}(\text{Mn}_{0.33}\text{Co}_{0.33}\text{Ni}_{0.33})\text{O}_2$ by airborne $\text{H}_2\text{O}/\text{CO}_2$ and inhibits the generation of residual sodium compounds (NaOH and Na_2CO_3) on the surface. The air/water stability of $\text{Na}_{0.4}(\text{Mn}_{0.33}\text{Co}_{0.33}\text{Ni}_{0.33})\text{O}_2$ is significantly improved, while the SnO coating reduces side reactions, facilitates the smooth transport of sodium ions, and improves its electrochemical performance. Conventional coating methods are usually unable to obtain a uniform thickness. In addition, thicker coatings in certain areas will affect sodium ion diffusion, increase impedance, and reduce discharge capacity. Therefore, there is an urgent need to develop a new coating technology to construct a protective layer with uniform and adjustable thickness. The atomic layer deposition (ALD) is a method of growing thin films in the vapour phase, which can precisely control the thickness of the coating layer at the atomic level to form a uniform coating layer. Sun et al.^[105] use ALD to construct a thin and uniform Fe_2O_3 coating layer on the surface of $\text{Na}_{0.75}\text{Ni}_{0.2}\text{Co}_{0.2}\text{Mn}_{0.6}\text{O}_2$, which significantly improves the structure and interfacial stability, as well as the long-term capacity/voltage cycling stability. Further, the in-situ construction coating layer is achieved through a chemical reaction between the medium and the residual sodium compounds, thus eliminating surface impurities, at the same time forming a protective layer on the surface of the cathode materials, and blocking $\text{H}_2\text{O}/\text{CO}_2$ in the air. Li et al.^[87] develop a thin and uniform LiF coating layer on the surface of $\text{Na}_{0.79}\text{Li}_{0.13}\text{Ni}_{0.2}\text{Mn}_{0.67}\text{O}_2$ (Na-LNM) by a one-step electrochemical in-situ coating method (Figure 9a), which mitigates the side reaction between Na-LNM and electrolyte, as well as achieves an ultra-long cycle for 1000 cycles at 1.5–4.5 V (Figure 9b).

4.3.3. Defects construction

In particular, Guo et al.^[36] introduce appropriate amount of Na vacancies into the O3-type cathode materials to increase the transition metal valence state, enhance the antioxidant capability of the materials and thus inhibit the reaction between the materials and water/carbon dioxide in the air. After the introduction of Na vacancies, the interlayer spacing increases, and the valence state of transition metal Ni increases, while the valence states of Fe and Mn remain basically unchanged (Figure 9c-f). By fitting the XPS results of C and O, it is shown that $\text{Na}_{0.93}\text{LNFM}$ reveals less surface residual alkalis (Figure 9g,h). Air stability tests of $\text{Na}_{0.93}\text{LNFM}$ and NaLNFM under the same conditions show that the structural decay of NaLNFM is more severe after exposure to air, and a significant loss of capacity is observed. By contrast, the $\text{Na}_{0.93}\text{LNFM}$ with Na vacancies is significantly improved. Noked et al.^[106] introduce Na vacancies in high-entropy cathode materials by Li doping, which not only increases the layer spacing, but also attenuates the shielding effect of sodium ions and improves the kinetic performance. Meanwhile, with the increase of transition metal oxidation states, the antioxidant capacity of high-entropy cathode materials is significantly improved. After 30 days of air exposure, no impurity is detected in the XRD test of the $\text{Na}_{0.9}\text{Li}_{0.1}$ cathode material (Figure 10a), confirming the stability of the crystal structure. The high-resolution transmission electron microscope (HRTEM) (Figure 10b) shows that the exposed $\text{Na}_{0.9}\text{Li}_{0.1}$ reveals a well-defined lattice edge in the (003) plane. The introduction of Na vacancies enables the cathode material to exhibit excellent air stability, which is an important factor for lowering the overall cathode storage cost. The comparison of modification strategies and performance is included in the Table 1 as follows. It lists the most recent modifications and the corresponding electrochemical performance.

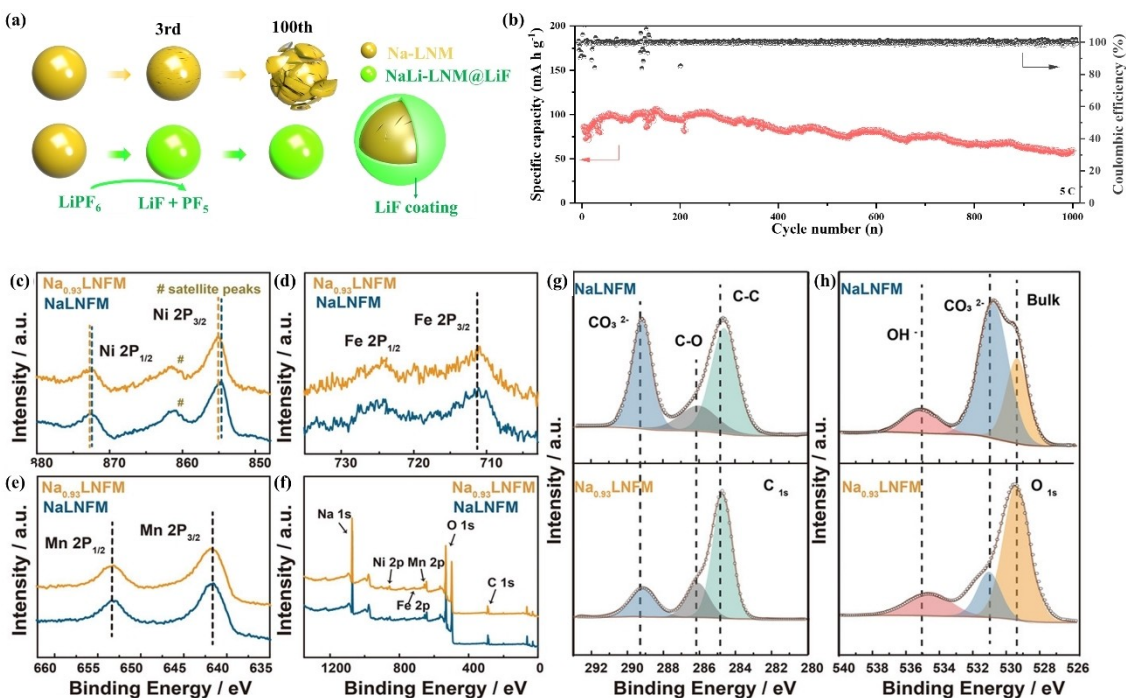


Figure 9. (a) The diagram of in-situ LiF coating. (b) The long-cycling performance of NaLi-LNM@LiF.^[87] Copyright 2022, Elsevier. Comparison of XPS spectra of Na_{0.93}LNFNM and NaLNFM for (c) Ni 2p, (d) Fe 2p, (e) Mn 2p. (f) XPS full spectrum analysis. XPS analysis of 9 g) C 1s and (h) O 1s, NaLNFM are displayed in the top and Na_{0.93}LNFNM are in the bottom.^[36] Copyright 2022, Wiley-VCH GmbH.

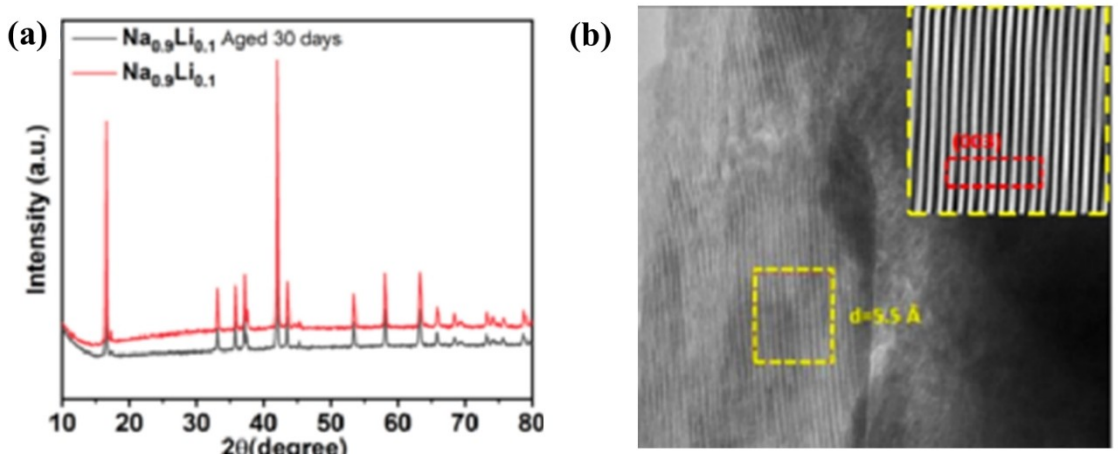


Figure 10. (a) XRD pattern of initial and aged Na_{0.9}Li_{0.1}. (b) HRTEM image of aged Na_{0.9}Li_{0.1}.^[106] Copyright 2023, Wiley-VCH GmbH.

In addition to the above three doping theories, washing and high-temperature calcination can also effectively remove impurities on the surface of materials. There are advantages and disadvantages of different modification strategies. Washing is not suitable for treating sodium ion layered oxides cathode materials. The Na_xTMO₂ is sensitive to H₂O, so post-treatment methods such as washing and coating methods involving aqueous solutions are not available. The high-temperature calcination is a general post-treatment method, a lot of materials can be heated to restore the performance. However, deterioration will still occur once the material is in contact with air again. Doping can improve the intrinsic air stability of

materials, which is a potential coping strategy. However, because the product properties are highly dependent on the synthesis methods and experimental conditions, the results of doping are usually unpredictable. It is still a great challenge to achieve targeted improvement of air stability through doping. Coating is a direct and effective strategy, but it requires the coating materials to possess the good ion conductivity and air stability at the same time, and to achieve the complete coating of materials, which is usually through a complex synthesis step. It also may be difficult to achieve in practical applications or lead to a significant increase in production costs. Therefore, the work related to the mechanism of air stability and inhibition of

Table 1. Comparison of modification strategies and electrochemical performance.

Cathode materials	Modification strategies	Capacity retention	Rate/cycle	Voltage (V)	Ref.
$\text{Na}_{0.98}\text{Ca}_{0.01}[\text{Ni}_{0.5}\text{Mn}_{0.5}]\text{O}_2$	Ca doping	67 %	0.5C/100	2.0-4.3	[101]
$\text{Na}_{0.80}\text{Li}_{0.13}\text{Ni}_{0.20}\text{Fe}_{0.1}\text{Mn}_{0.57}\text{O}_2$	Fe doping	75 %	1C/100	2.0-4.5	[99]
$\text{Na}_{0.4}(\text{Mn}_{0.33}\text{Co}_{0.33}\text{Ni}_{0.33})\text{O}_2@\text{Sno}$	SnO coating	69 %	0.5C/100	1.0-3.5	[90]
$\text{Na}_{0.66}\text{Li}_{0.18}\text{Fe}_{0.12}\text{Mn}_{0.7}\text{O}_2$	Li doping	87 %	0.05C/80	1.5-4.5	[107]
$\text{NaNi}_{0.45}\text{Mn}_{0.4}\text{Ti}_{0.1}\text{Co}_{0.05}\text{O}_2-\text{LiF}$	LiF coating	60 %	0.5C/200	2.0-4.4	[108]
$\text{Na}_{0.67}\text{Zn}_{0.1}\text{Mn}_{0.9}\text{O}_2@\text{Al}_2\text{O}_3$	Al_2O_3 coating	83 %	0.05C/130	2.0-4.4	[83]
$\text{Na}_{0.649}\text{Al}_{0.096}\text{Mn}_{0.826}\square_{0.078}\text{O}_2$	Introduction vacancies	69 %	1C/100	2.0-4.5	[69]
$\text{Na}_{2/3}\text{Li}_{1/6}\text{Co}_{1/6}\text{Mn}_{2/3}\text{O}_2$	Li/Co doping	95.8 %	1C/250	2.0-4.5	[109]
$\text{Na}_{0.7}\text{Li}_{0.03}[\text{Mg}_{0.15}\text{Li}_{0.09}\text{Mn}_{0.75}]\text{O}_2$	Li doping	80.9 %	0.5C/50	1.5-4.6	[57]
$\text{Na}_{0.67}\text{Ni}_{0.3}\text{Co}_{0.1}\text{Mn}_{0.6}\text{O}_{1.94}(\text{BO}_3)_{0.02}$	B doping	80 %	2C/1000	2-4.1	[110]
$\text{LiNi}_{0.83}\text{Co}_{0.06}\text{Mn}_{0.10}\text{Al}_{0.005}\text{Sm}_{0.005}\text{O}_2$	Al/Sm doping	91 %	1C/100	2.75-4.3	[111]
$\text{Na}_{0.5}\text{Li}_{0.1}\text{Ni}_{0.4}\text{Fe}_{0.2}\text{Mn}_{0.4}\text{Ti}_{0.04}\text{Mn}_{0.04}\text{Mg}_{0.02}\text{O}_{1.9}\text{F}_{0.1}$	Introduction vacancies	90 %	0.5C/200	2-4	[106]

surface impurity generation in layered transition metal oxide cathode materials for sodium ion batteries still needs to be vigorously explored.

5. Jahn-Teller effect

Jahn and Teller formulate the famous Jahn-Teller effect in 1937. It states that in symmetric nonlinear molecules, if the ground state of the system possesses more than one degenerate energy levels, there will occur spontaneous distortions which can eliminate degenerate energy levels. degenerate energy levels elimination can lead to symmetry and energy reductions in the system, so the Jahn-Teller effect is usually spontaneous. In sodium ion battery cathode materials, manganese-based materials are often prone to the Jahn-Teller effect. In the nonlinear MnO_6 octahedron, the high-spin state Mn^{3+} possesses a very large magnetic moment and only one electron in the doubly-degenerated eg-orbital of leading to an asymmetric distribution of electrons. The electrons in the $d_{x^2-y^2}$ and d_{z^2} orbitals exhibit different degrees of shielding to the Mn nucleus in different directions. However, in order to stabilize the migration of Mn^{3+} within the molecule, the longitudinal Mn–O bonds will gradually elongate and the horizontally oriented Mn–O bonds will shorten, thus causing the linear MnO_2 arrangement to elongate along the axial direction, giving rise to the Jahn-Teller distortion.

The Jahn-Teller effect may cause drastic structural changes as well as transition metals migration and dissolution. Fe, Mn and Ni are elements with Jahn-Teller effect, and they also elements that tend to migrate and dissolve. Here, taking Fe as an example, the reasons of elements migration and dissolution caused by Jahn-Teller effect is presented. As shown in Figure 11, when Fe independently exists in the transition metal layer, an increase of at least 0.7 eV in unit cell energy is required if it migrates from the octahedral position of the transition metal layer to the tetrahedral interstitial position of the sodium layer. However, when a number of Fe atoms form clusters, the energy

required for migration significantly decreases.^[112] When Fe^{4+} with Jahn-Teller effect clusters together, Fe in the transition metal layer can adapt to the shortening of the surrounding Fe–O bond, and this effect can significantly reduce the energy of the tetrahedral sites of the sodium layer, thus greatly increasing the rate of Fe migration. This result also indicates that the Fe content of the transition metal layer should not exceed 1/3. Moreover, reducing the content of Fe, Mn and Ni in the transition metal layer by elements doping, or changing the valence state of Fe^{4+} or Mn^{3+} by introducing defects can reduce the ions with the Jahn-Teller effect.

Wang et al.^[113] design P2- $\text{Na}_{2/3}[\text{Zn}_{1/9}\text{Mn}_{7/9}\square_{1/9}]\text{O}_2$ (NZMO-VAC) with vacancies and P2- $\text{Na}_{2/3}[\text{Zn}_{2/9}\text{Mn}_{7/9}]\text{O}_2$ (NZMO) without vacancies to elucidate how vacancies can modulate the rotational state of Mn^{3+} and enhance the structural stability. On the one hand, the introduction of vacancies in the transition metal layer raises the valence of manganese ions, enhances the ordered arrangement of $\text{Mn}/\text{Zn}/\square$, and promotes the anion redox capacity and its reversibility. On the other hand, transition metal vacancies alter the rotational state of Mn^{3+} and increase the proportion of low-spinning Mn^{3+} in $\text{Na}_{2/3}[\text{Zn}_{1/9}\text{Mn}_{7/9}\square_{1/9}]\text{O}_2$ by shortening the length of the MnO bond during discharging. Guo et al.^[114] dope divalent Zn into P2- $\text{Na}_{0.833}[\text{Li}_{0.25}\text{Mn}_{0.75}]\text{O}_2$ to replace the Mn site. P2- $\text{Na}_{0.833}\text{Zn}_{0.0375}[\text{Li}_{0.25}\text{Mn}_{0.7125}]\text{O}_2$ is prepared by the sol-gel method combined with heat treatment. Zn doping not only increases the average oxidation state of Mn to mitigate the Jahn-Teller effect, but also reduces structural changes and instabilities.

6. Transition metal migration and dissolution

6.1. Hazards of transition metal dissolution

Transition metal ions dissolution is a common problem in lithium-ion batteries and sodium-ion batteries.^[115] Generally, transition metals such as Ni and Mn, which have the Jahn-Teller effect, are more prone to dissolution compared with Co.^[116,117]

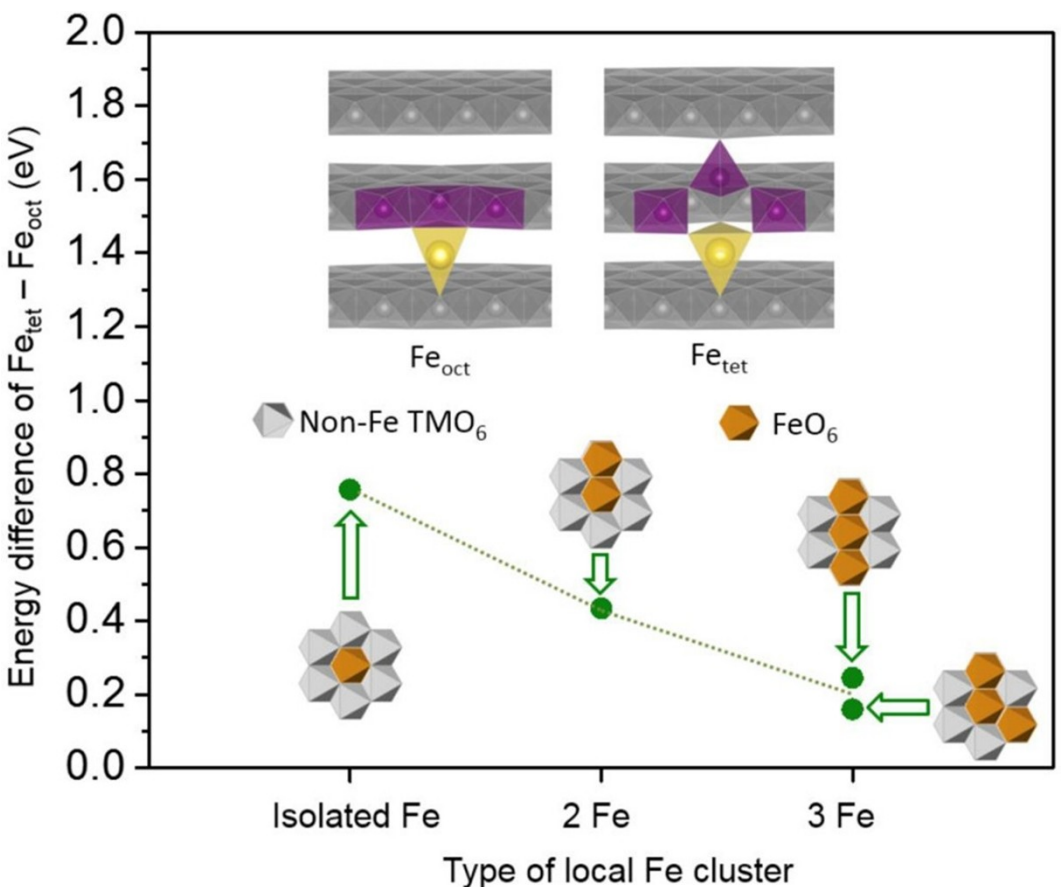


Figure 11. The energy difference for Fe migration through the octahedral position of the transition metal layer to the tetrahedral position of the sodium layer.^[112] Copyright 2016 American Chemical Society

Dissolved transition metal ions will migrate to the negative electrode and be deposited on the negative electrode side, which will not only cause an increase in the thickness of the fixed electrolyte interphase (SEI) film on the negative electrode side,^[118,119] reduce the activated Na^+ , and increase the internal resistance of the battery, but also continue to catalyse the decomposition of the electrolyte and reduce the cycle life of the battery.^[115]

In early studies of layered oxides for sodium-ion batteries, it was found that the reversible specific capacity of Na_xFeO_2 and Na_xCrO_2 decreases rapidly and is accompanied by a significant increase in voltage hysteresis after the removal of sodium content greater than 0.5. Results such as XRD, Musburger spectroscopy of ^{57}Fe , and HRTEM have demonstrated that there is an irreversible migration of transition metal ions to the sodium layer in these two materials. Figure 12a shows a schematic diagram of the migration process of transition metal ions. The irreversible migration of the transition metal hinders the re-embedding of Na^+ during the discharge process, and thus exhibits a large voltage hysteresis and a low reversible specific capacity. The irreversible Fe migration of NaFeO_2 after charging to 4.4 V can be clearly observed by spherical aberration-corrected transmission electron microscopy (AC-TEM), as shown in Figure 12b,c. In order to reduce the migration

of transition metals, doping substitution or coating is generally used.

6.2. Modification strategies for transition metal dissolution

Wang et al.^[120] construct a 5 nm Al_2O_3 coating layer on the surface of $\text{Na}_{0.67}\text{MnO}_2$ by using ALD technology, which effectively mitigates the volume change of the particles and the Mn dissolution, as well as enhances the electrochemical performance of cathode materials. As shown in Figure 12d, pure $\text{Na}_{0.67}\text{MnO}_2$ particles (Figure 12d-1) and particles cycled at 3.8 V (Figure 12d-2) for 30 cycles exhibit similar layered structures, indicating negligible structural changes or Mn^{2+} dissolution within the narrow cut-off window, whereas distinct corrosion regions can be observed in particles cycled at 4.3 V (Figure 12d-3) for 30 cycles, suggesting that extended cut-off window intensifies Mn^{2+} dissolution. In addition, due to the volume expansion during the sodiation/de-sodiation process, significant cracks are formed at the expansion cut-off window of 30 cycles (Figure 12d-4), which promotes Mn^{2+} dissolution. Therefore, XRD and HRTEM results indicate that the volume expansion and disproportionation of Mn^{3+} are the main reasons for the capacity decay of $\text{Na}_{0.67}\text{MnO}_2$ electrode. Wei et al.^[121] construct a MgO coating layer on the surface of P2/P3-

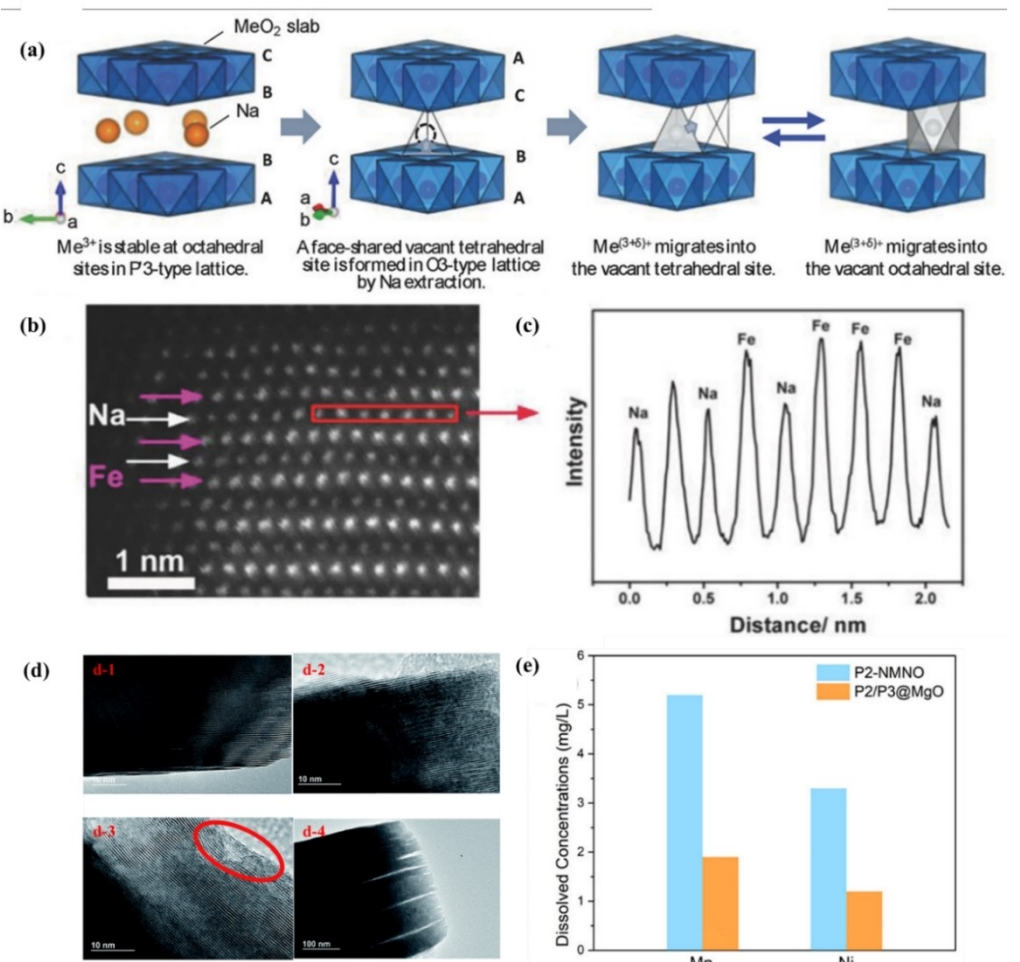


Figure 12. (a) Mechanism of transition-metal migration on the sodium extraction process. (b) HAADF images of NaFeO_2 at the fully charged state and (c) the corresponding line profile acquired from the red rectangular region in (b). (d) HRTEM images for the (d-1) fresh $\text{Na}_{0.67}\text{MnO}_2$ electrode and (d-2) $\text{Na}_{0.67}\text{MnO}_2$ electrodes after 30 cycles with the narrow cutoff window. HRTEM images for the (d-3) fresh $\text{Na}_{0.67}\text{MnO}_2$ electrode and (d-4) $\text{Na}_{0.67}\text{MnO}_2$ electrodes after 30 cycles with the expanded cutoff window.^[120] Copyright 2017, Royal Society of Chemistry. (e) Mn and Ni concentrations in the electrolyte of two electrodes.^[121] Copyright 2022, American Chemical Society.

$\text{Na}_{0.67}\text{Mn}_{0.67}\text{Ni}_{0.33}\text{O}_2$, and ICP tests show that the coating layer effectively suppresses the transition metals (Mn and Ni) dissolution (Figure 12e). This result verifies that the construction of the surface coating layer shows a positive effect on the suppression of the transition metal ions dissolution. Xiao et al.^[122] use ALD coating effectively inhibits the cathode surface side reactions and transition metal leaching of P3/P2- $\text{Na}_{2/3}\text{Ni}_{1/3}\text{Mn}_{2/3}\text{O}_2$, as shown in Figure 13a, thus providing superior protection, and the capacity retention of P3/P2- $\text{Na}_{2/3}\text{Ni}_{1/3}\text{Mn}_{2/3}\text{O}_2\text{-Al}_2\text{O}_3$ ALD is as high as 87% after 300 cycles at 5 C.

In addition, besides the construction of surface coatings, the dissolution of transition metals can also be effectively suppressed by elemental doping or introduction of defects to dilute transition metal ions with Jahn-Teller effect, limiting the charging voltage or improving the high-voltage resistance property of the electrolyte, and using water-removing additives, which can be used to block the reactive generation path of HF.

Zhou et al.^[123] successfully prepare superlattice-ordered $\text{Na}_3\text{Ni}_2\text{RuO}_6$ using a simple solid-phase sintering method. In the

transition metal layer of the ordered $\text{Na}_3\text{Ni}_2\text{RuO}_6$, the ordered arrangement of transition metal ions leads to interaction forces between the transition metal ions, which in turn strengthens the layered structure and alleviates the migration of transition metal cations. Ultimately, the $\text{Na}_3\text{Ni}_2\text{RuO}_6$ exhibits an ultra-long potential plateau, high reversible specific capacity and excellent cycling performance. In order to further improve the development of LTMOs. Sun et al.^[124] report a multi-element (Fe/Mg/Li) co-doping strategy to develop a novel P2/O3 biphasic cathode material for SIBs. Since high-spin Mn^{3+} induces the Jahn-Teller effect, appropriate heteroatom substitution is expected to improve the structural stability and reduce the dissolution of the TMO₂ layer. Due to the presence of low oxidation states Li^+ and Mg^{2+} in the transition metal layer, the peak in the Mn 2p (Figure 13b) in the doped sample is located at a higher binding energy, indicating that the average oxidation state of Mn in $\text{Na}_{2/3}\text{Ni}_{2/9}\text{Mn}_{5/9}\text{Fe}_{1/9}\text{Mg}_{1/9}\text{O}_2$ (NMFNM) and $\text{Na}_{2/3}\text{Ni}_{2/9}\text{Mn}_{5/9}\text{Fe}_{1/9}\text{Mg}_{1/9}\text{O}_2$ (NMFML) is higher than that in the original sample. After cycling, XPS analysis in the Figure 13c,d demonstrates that the

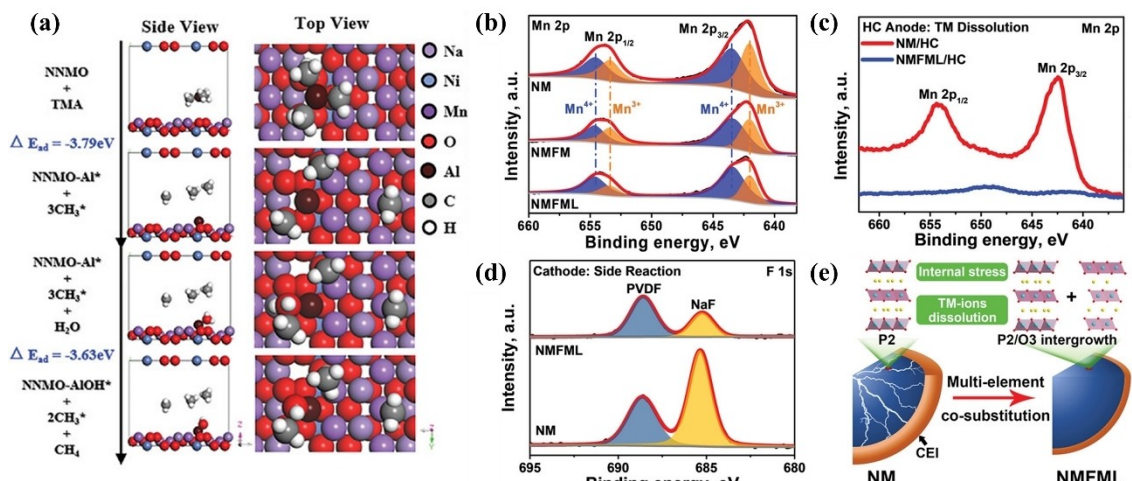


Figure 13. (a) Schematic diagram of the first ALD process of Al_2O_3 on the surface of the NNMO simulated with first principles.^[122] Copyright 2022, Wiley-VCH. (b) High-resolution Mn 2p XPS spectra of NM, NMFML, and NMFML. (c) Mn 2p XPS spectra of cycled HC anodes recovered from NM/HC and NMFML/HC Na full cells. (d) F 1s XPS spectra of cycled NM and NMFML cathodes. (e) Schematic illustration of the structural evolution of NM and NMFML cathodes during cycling.^[124] Copyright 2022, Wiley-VCH.

multi-element co-substitution strategy effectively suppress the dissolution of active materials and harmful parasitic reactions, thus limiting the degradation of cathode materials and electrolytes, which is the key to prolong the cycle life of sodium-ion batteries. As a result, the NMFML exhibits extended cycle life (71.8% capacity retention after 500 cycles at 5 C) and excellent rate performance (106.6 mA h g^{-1} at 10 C).

7. Crystal structure evolution

7.1. Mechanism and type of phase transition

The phase transition is one of the main reasons for the continuous decline in the electrochemical performance of sodium-ion batteries. As shown in Figure 14a, the repulsive force of the adjacent oxygen layer gradually increases with the sodium ion detachment.^[125] In the interval of lower sodium content (higher voltage), the adjacent TMO_2 layer slips to balance the increased O–O repulsive force, thus gradually transforming from P to O structure (Figure 14b).

Phase transition frequently occurs in the electrochemical processes of O3-type Na_xTMO_2 materials, comprising the O3 phase to the P3 phase, further to a new O3 phase or OPn phase or O1 phase during charging, as well as the O3 phase to the lattice-distorted O'3 phase during discharging. In addition to phase transition in the crystal structure of the O3 phase, the common structural transition of the O3 phase can be divided into two steps: From O3 to P3 at 4 V and from P3 to O1 at a higher voltage during charging. Moreover, there may be an intermediate phase of O'3 and P'3, respectively, during these two steps. For example, the O3- $\text{Na}[\text{Ni}_{0.60}\text{Fe}_{0.25}\text{Mn}_{0.15}]\text{O}_2$ ^[126] shows poor sodium ion diffusion kinetic properties and thermodynamic stability of O3'' although it is accompanied by a reversible

phase transition process of O3-O'3-P3-O3'' during Na de-embedding.

7.2. Strategies of inhibiting phase transition

The current strategies to mitigate the P–O phase transition mainly include doping, introducing TM vacancies and adjusting the layer spacing of the Na^+ layer. For example, the introduction of Zn, Fe, and Al into P2- $\text{Na}_{0.67}\text{Ni}_{0.33}\text{Mn}_{0.67}\text{O}_2$ can transform P2-O2 into P2-OP4 phase transition with small volume changes. The introduction of an appropriate amounts of vacancies can effectively buffer the structural changes brought by the P–O phase transition. In addition, by increasing the layer spacing of the AM layer, the repulsive force between O–O can be effectively reduced to alleviate the structural changes.

7.2.1. Elements doping

Wu et al.^[127] significantly enhance the crystal and surface interface structure stability by simultaneously constructing a surface ZrO_2 coating and bulk phase Zr^{4+} doping in P2- $\text{Na}_{2/3}\text{Ni}_{1/3}\text{Mn}_{2/3}\text{O}_2$ cathode materials based on solid state physics theory, increasing the impurity-vibrational entropy of the cathode materials. The in-situ XRD tests show that the Zr modification significantly enhances the stability of the crystal structure of LTMOs and effectively suppress the P2-O2 phase transition (Figure 14c,d). After complete sodiation, the P2- $\text{Na}_{2/3}\text{Ni}_{1/3}\text{Mn}_{2/3}\text{O}_2$ suffers from intense cell shrinkage (13.5%), which severely damages the crystal structure and produces grain cracks. In contrast, the rate of change in the cell volume of the Zr-modified cathode material is only 1.18% (Figure 14e), and the crystal structure of the material remains intact after cycling. Guo

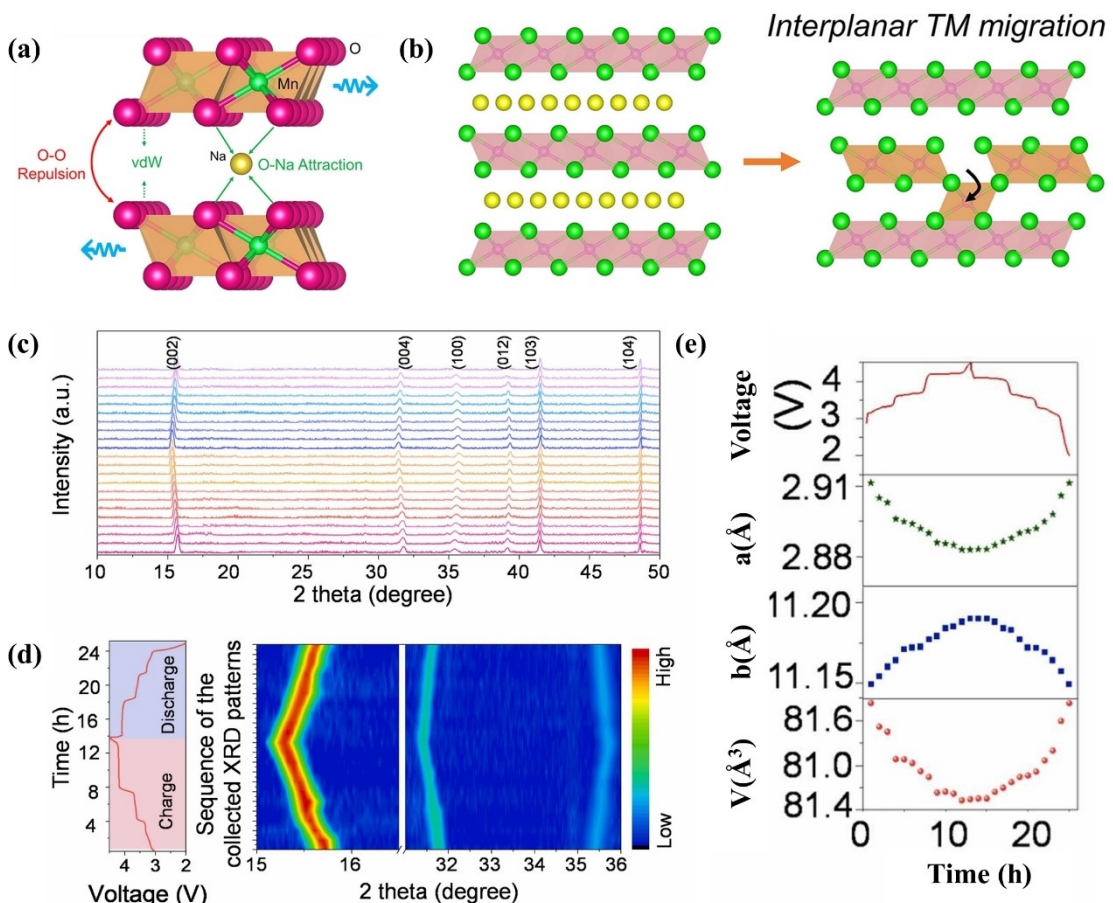


Figure 14. (a) Schematic illustration of interlayer gliding (P–O transformations). (b) Schematic illustration of interplanar TM migration.^[125] Copyright 2022, American Chemical Society. (c) In-situ XRD patterns of P2-NaNM@Zr electrode during the first charge/discharge process at 30 mA g^{-1} and (d) the corresponding charge/discharge profile and the selected (002), (004), (100) diffraction profiles. (e) Lattice parameter evolution of P2-NaNM@Zr electrode during the first charge/discharge process.^[127] Copyright 2022, Elsevier.

et al.^[128] use the synergistic effect of Li^+ , Mg^{2+} and Ti^{4+} to increase the slip energy barrier of the TM layer for $\text{P2-Na}_{2/3}\text{Ni}_{1/3}\text{Mn}_{2/3}\text{O}_2$ during the de-embedding process, and transform the original P2-O2 bulk violent phase transition (volumetric change is 19.4%) into a highly reversible P2-Z mild phase transition process (volumetric change is 2.5%) to achieve a substantial increase in the cycling stability of SIBs.

The Na^+ locate at a trigonal position for the P3 phase and the interlayer spacing of the transition metal layer is wide. Compared with the O3 phase, the diffusion energy barrier of Na^+ in the P3 phase is lower, possessing the potential advantage to be the excellent cathode materials for sodium ion batteries. Lu et al.^[129] design the zero-strain P3- $\text{Na}_{0.75}\text{Mg}_{0.08}\text{Co}_{0.10}\text{Ni}_{0.2}\text{Mn}_{0.60}\text{O}_2$ (P3-MNCM) layered oxide as a cathode material for sodium-ion batteries by Mg doping. As shown in Figure 15, P3-MNCM reveals less than 1.4% cell volume deformation during sodium de-embedding in the voltage range 2.0–4.3 V. DFT calculations show that Mg doping can effectively mitigate the Jahn-Teller effect of Ni^{3+} at the high voltage. The electrochemically inactive Mg in the transition metal layer can effectively block the local conduction of

octahedral distortion, thus effectively improving the stability of the P3-type structure.

7.2.2. Construct particular structure

Zhou et al.^[130] successfully prepare the three-phase cathode material P3/P2/O3- $\text{Na}_{0.674}\text{Ni}_{0.319}\text{Mn}_{0.590}\text{O}_2$ (P3/P2/O3-NNMO) by changing the calcination conditions (temperature and atmosphere) with the same stoichiometric ratios of the transition metal oxalates and Na_2CO_3 as raw materials without introducing the doping element. The structural evolution of the composite phase materials is investigated using ex-situ XRD (Figure 16d), and it is found that upon charging to 4.2 V, both P2/P3-NNMO and P3/P2-NNMO undergo an irreversible P2-O2 phase transition, which maybe generate a huge strain and volume contraction, easily leading to the deactivation of the active materials. On the other hand, P3/P2/O3-NNMO does not undergo the irreversible P2-O2 phase transition in the high-voltage region, and it can be restored to the initial P3/P2/O3 three-phase structure in the end state of the discharge, which indicates a good structural reversibility, as shown in the

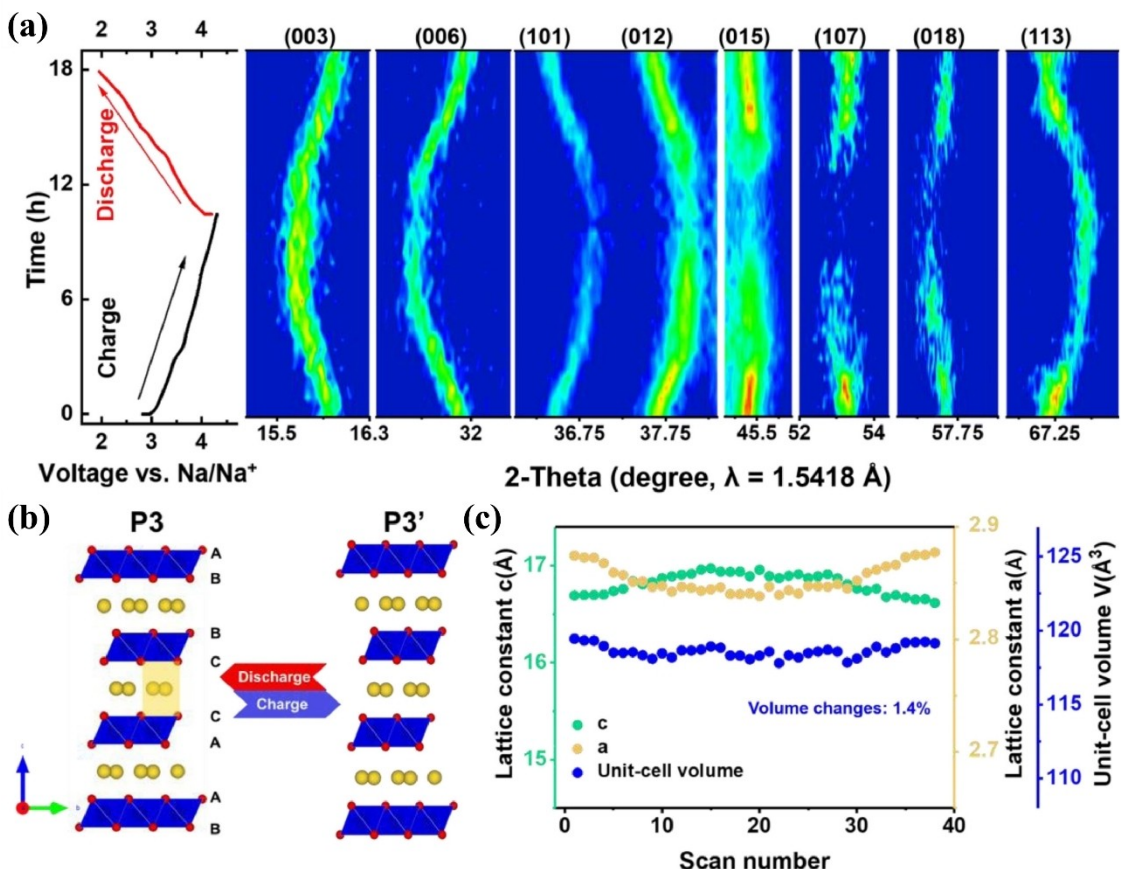


Figure 15. Structural evolution of P3-MNCM electrode. (a) The intensity contour maps of P3-MNCM cathode using in-situ XRD patterns during the formation cycle; (b) Schematic representation of phase transition of P3-MNCM electrode upon Na^+ extraction/insertion; (c) The variations of unit cell volume V and lattice constants a and c , which are determined from the in-situ XRD results.^[129] Copyright 2021 Elsevier B.V.

structural evolution diagram of Figure 16a-c. The staggered individual structures in the P3/P2/O3-NNMO make the TMO_2 slip in different directions during the charging/discharging. Moreover, the phase transition voltages of the different structures are different, which means that the P2 and P3 phases remain unchanged during the transition from the O3 phase to the P3 phase at the beginning of the charging. Due to the mutual “structural confinement effect”, the adjacent and different structures inhibit the consecutive slippage of the TMO_2 layer, which is conducive to the maintenance of the structural stability.

Yang et al.^[84] employ a treatment method using water as a medium to effectively inhibit the phase transition of Mn-based Na_xTMO_2 . The Na^+ layer spacing is enlarged from 3.6 Å to 3.8–5.8 Å by the aqueous treatment. The final product (S-NMO) shows a shale-like structure with an accordion-like morphology (Figure 16e). After 100 cycles at 2.0–4.4 V, the capacity retention of the cathode material increases from 41% for the initial $\text{Na}_{0.67}\text{MnO}_2$ to 99% for S-NMO, indicating the excellent electrochemical stability of S-NMO. The synchrotron in situ XRD pattern in Figure 16f shows that S-NMO does not undergo significant P-O or P'2-P2 phase transitions in the voltage range of 2.0–4.45 V. The S-NMO is also a good candidate for the P-O or P'2-P2 phase transition. Its 1.96% volume change (Fig-

ure 16g) arises from the respiratory effect induced by the redox reaction of Mn ions. Figure 16h shows that all the diffraction peaks in the charging or discharging states with different number of cycles are in good agreement, demonstrating the excellent structural reversibility of S-NMO during cycling. These results confirm that increasing the Na^+ layer spacing is an effective way to suppress the phase transition and improve the electrochemical performance.

P3-type layered oxides with larger channels allow for fast Na^+ transport and thus show great rate performance. However, the lower crystal symmetry of the P3-type oxides and the change in Na^+ content in the Na layer during charging/discharging process lead to a large variation in the electrostatic repulsion between the TMO_2 plates, resulting in an irreversible phase transition. LEE et al.^[131] discover the Na^+ conductor Na_2SeO_4 , which can easily in situ grow on the P3- $\text{Na}_{0.45}\text{Ni}_{0.2}\text{Mn}_{0.8}\text{O}_2$ to form the novel P3- $\text{Na}_{0.45}\text{Ni}_{0.2}\text{Mn}_{0.8}\text{O}_2/\text{Na}_2\text{SeO}_4$ with the heterostructure. The synergistic interaction between P3- $\text{Na}_{0.45}\text{Ni}_{0.2}\text{Mn}_{0.8}\text{O}_2$ and Na_2SeO_4 promotes Na^+ diffusion and inhibits the P3-O3 phase transition during deep sodiation, resulting in a high rate performance and excellent cycling stability.

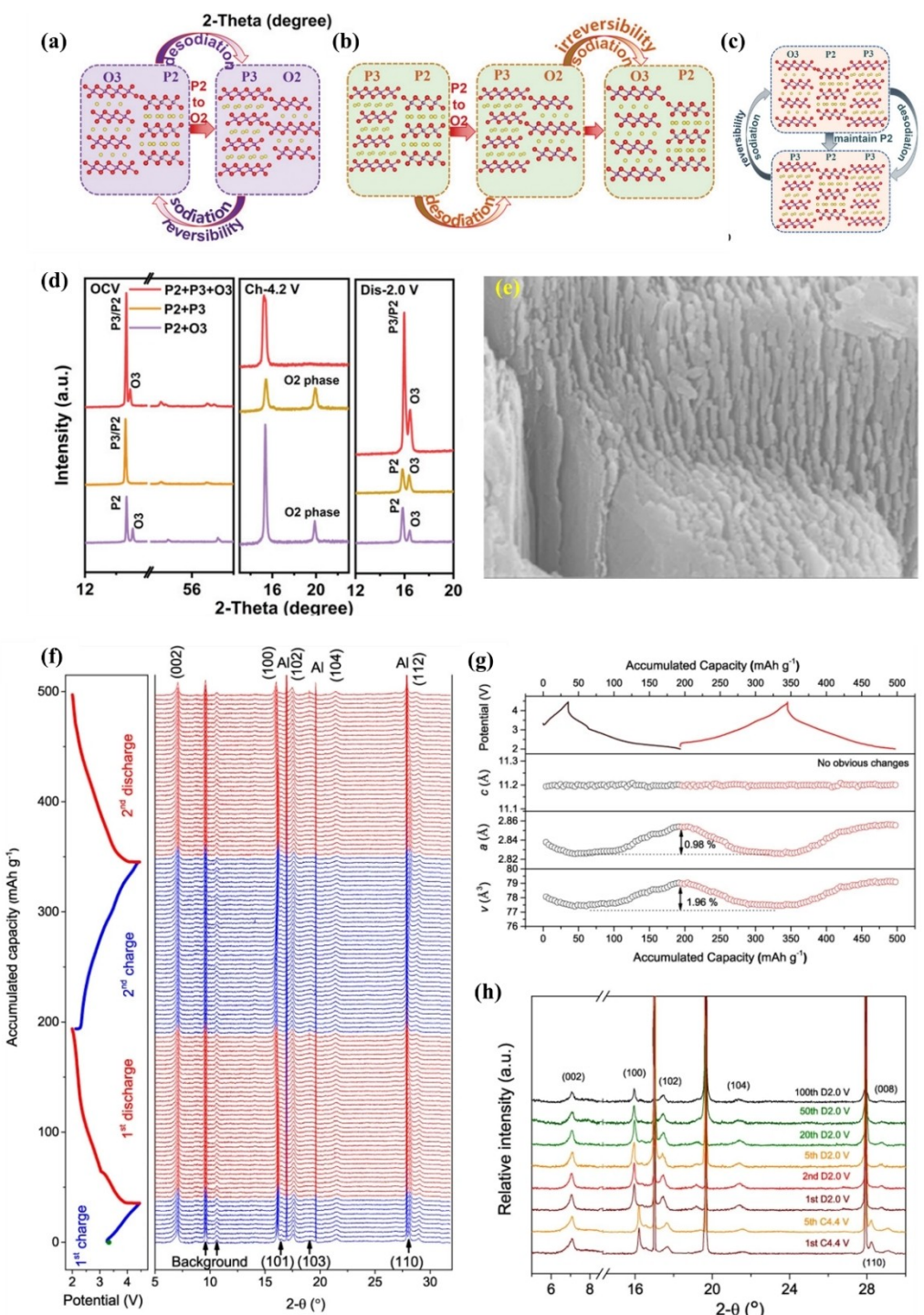


Figure 16. Corresponding crystal structure evolution of (a) P3/P2/O3-NNMO, (b) P2/O3-NNMO, and (c) P3/P2-NNMO in the charge/discharge process. (d) Comparison of phase transformation among P3/P2/O3-NNMO, P3/P2-NNMO, and P2/O3-NNMO (OCV: open circuit voltage pris, Ch-4.2 V: charge to 4.2 V, Dis-2.0 V: discharge to 2.0 V).^[130] Copyright 2022, Wiley-VCH. (e) The SEM image of S-NMO. (f) The in situ XRD patterns (g) calculated lattice parameters. (h) The comparison of XRD patterns of S-NMO at different cycles.^[84] Copyright 2021, The Author(s).

8. Summary and outlook

Layered transition metal oxide cathode materials for sodium-ion batteries have received extensive attention from researchers for their low price and relatively high specific capacity. With the in-depth study, the constitutive relationship of layered oxide

cathode materials has been gradually clarified. Based on the constitutive relationship and failure mechanism, researchers have adopted a series of modification means to modify the layered oxide cathode materials, including the introduction of new elemental doping, multiphase composites, and the means of coating and micro-control of the structure and other means

to achieve significant result. However, in terms of structural stability and electrochemical performance, there is still a gap with lithium-ion battery cathode materials. The poor air stability, irreversible loss of lattice oxygen, and Na^+ /vacancy ordering transition are still the key problems of layered oxide cathode materials, which need to be explored in order to deeply reveal the mechanisms at the atomic and molecular levels. In the future, in-depth study of the existing problems is indispensable, and the redox mechanism and process of lattice oxygen should be further investigated, and how to effectively break the Na^+ /vacancy ordering transition is also one of the core problems of the study. For the phenomena that cannot be explained by existing theories, we should also explore the mechanism of its action, and analyse its nature, structure and law of change from the perspective of atomic and ionic action, which is the key point to break through the common action of multiple metal oxides. The use of synergistic effect and the exploration of new structure-effect relationship is the way to push the sodium-ion batteries to large-scale commercialisation.

Acknowledgements

This work is financially supported by the National Natural Science Foundation of China (Grants 51972023).

Conflict of Interests

The authors declare that they have no known competing financial interests or personal relationships that could have appeared to influence the work reported in this paper.

Keywords: degradation mechanisms • layered transition metal oxides cathodes • modification strategies • sodium ion batteries • structural stability

- [1] J. Zhang, J. Gai, K. Song, W. Chen, *Cell Rep. Phys. Sci.* **2022**, *3*, 100868.
- [2] A. Rudola, R. Sayers, C. J. Wright, J. Barker, *Nat. Energy* **2023**, *8*, 215–218.
- [3] Z. Lv, H. Xu, W. Xu, B. Peng, C. Zhao, M. Xie, X. Lv, Y. Gao, K. Hu, Y. Fang, W. Dong, F. Huang, *Adv. Energy Mater.* **2023**, *13*, 2300790.
- [4] X. Song, X. Li, H. Shan, J. Wang, W. Li, K. Xu, K. Zhang, H. M. K. Sari, L. Lei, W. Xiao, J. Qin, C. Xie, X. Sun, *Adv. Funct. Mater.* **2023**, 2303211.
- [5] T. Yang, Y. Huang, J. Zhang, H. Zhu, J. Ren, T. Li, L. C. Gallington, S. Lan, L. Yang, Q. Liu, *J. Energy Chem.* **2022**, *73*, 542–548.
- [6] H. Li, Y. Wang, X. Zhao, J. Jin, Q. Shen, J. Li, Y. Liu, X. Qu, L. Jiao, Y. Liu, *ACS Energy Lett.* **2023**, *8*, 3666–3675.
- [7] P. Zhou, J. Zhang, Z. Che, Z. Quan, J. Duan, X. Wu, J. Weng, J. Zhao, J. Zhou, *J. Energy Chem.* **2022**, *67*, 655–662.
- [8] X. Liang, J.-Y. Hwang, Y.-K. Sun, *Adv. Energy Mater.* **2023**, *13*, 2301975.
- [9] M. S. Chae, H. J. Kim, H. Bu, J. Lyoo, R. Attias, B. Dlugatch, M. Oliel, Y. Gofer, S.-T. Hong, D. Aurbach, *Adv. Energy Mater.* **2020**, *10*, 2000564.
- [10] R. Yu, Z. Zhang, S. Jamil, J. Chen, X. Zhang, X. Wang, Z. Yang, H. Shu, X. Yang, *ACS Appl. Mater. Interfaces* **2018**, *10*, 16561–16571.
- [11] J. Feng, S. Luo, J. Cong, K. Li, S. Yan, Q. Wang, Y. Zhang, X. Liu, X. Lei, P. Hou, *Electroanal. Chem.* **2022**, *916*, 116378.
- [12] L. Deng, G. Sun, K. Goh, L.-L. Zheng, F.-D. Yu, X.-L. Sui, L. Zhao, Z.-B. Wang, *Electrochim. Acta* **2019**, *298*, 459–467.
- [13] Y. Jiang, X. Zhou, D. Li, X. Cheng, F. Liu, Y. Yu, *Adv. Energy Mater.* **2018**, *8*, 1800068.

- [14] H. J. Song, J.-C. Kim, M. A. Dar, D.-W. Kim, *J. Power Sources* **2018**, *377*, 121–127.
- [15] S. Qiu, Y. Xu, X. Wu, X. Ji, *Electrochem. Energy Rev.* **2022**, *5*, 242–262.
- [16] X. Gao, F. Jiang, Y. Yang, Y. Zhang, G. Zou, H. Hou, Y. Hu, W. Sun, X. Ji, *ACS Appl. Mater. Interfaces* **2020**, *12*, 2432–2444.
- [17] H. Yi, R. Qin, S. Ding, Y. Wang, S. Li, Q. Zhao, F. Pan, *Adv. Funct. Mater.* **2021**, *31*, 2006970.
- [18] H. Zhang, Y. Gao, X.-H. Liu, Z. Yang, X.-X. He, L. Li, Y. Qiao, W.-H. Chen, R.-H. Zeng, Y. Wang, S.-L. Chou, *Adv. Funct. Mater.* **2022**, *32*, 2107718.
- [19] C. A. R. Júnior, E. R. Sanseverino, P. Gallo, D. Koch, Y. Kotak, H.-G. Schweiger, H. Zanin, *J. Energy Chem.* **2023**, *78*, 507–525.
- [20] H. Zhu, Z. Yao, H. Zhu, Y. Huang, J. Zhang, C. C. Li, K. M. Wiaderek, Y. Ren, C.-J. Sun, H. Zhou, L. Fan, Y. Chen, H. Xia, L. Gu, S. Lan, Q. Liu, *Adv. Sci.* **2022**, *9*, 2200498.
- [21] C. Delmas, C. Fouassier, P. Hagenmuller, *Physica B+C* **1980**, *99*, 81–85.
- [22] X.-H. Ma, Le-Le Li, Long Cheng, Fan Qiao, *J. Alloys Compd.* **2020**, *36*, 623–628.
- [23] S. G. Lim, M.-S. Kwon, T. Kim, H. Kim, S. Lee, J. Lim, H. Kim, K. T. Lee, *ACS Appl. Mater. Interfaces* **2022**, *14*, 33120–33129.
- [24] C. Chen, W. Huang, Y. Li, M. Zhang, K. Nie, J. Wang, W. Zhao, R. Qi, C. Zuo, Z. Li, H. Yi, F. Pan, *Nano Energy* **2021**, *90*, 106504.
- [25] W. Xu, R. Dang, L. Zhou, Y. Yang, T. Lin, Q. Guo, F. Xie, Z. Hu, F. Ding, Y. Liu, Y. Liu, H. Mao, J. Hong, Z. Zuo, X. Wang, R. Yang, X. Jin, Y. Lu, X. Rong, N. Xu, Y.-S. Hu, *Adv. Mater.* **2023**, *35*, 2301314.
- [26] M. Chen, Q. Liu, S.-W. Wang, E. Wang, X. Guo, S.-L. Chou, *Adv. Energy Mater.* **2019**, *9*, 1803609.
- [27] T. Wang, D. Su, D. Shanmukaraj, T. Rojo, M. Armand, G. Wang, *Electrochem. Energy Rev.* **2018**, *1*, 200–237.
- [28] Q. Yang, P.-F. Wang, J.-Z. Guo, Z.-M. Chen, W.-L. Pang, K.-C. Huang, Y.-G. Guo, X.-L. Wu, J.-P. Zhang, *ACS Appl. Mater. Interfaces* **2018**, *10*, 34272–34282.
- [29] X. Liu, Guiming Zhong, Zhumei Xiao, Bizi Zheng, Wenhua Zuo, Yong Yang, *Nano Energy* **2020**, *76*, 104997.
- [30] Y. Liu, Q. Shen, X. Zhao, J. Zhang, X. Liu, T. Wang, N. Zhang, L. Jiao, J. Chen, L. Fan, *Adv. Funct. Mater.* **2020**, *30*, 1907837.
- [31] Y.-J. Guo, P.-F. Wang, Y.-B. Niu, X.-D. Zhang, Q. Li, X. Yu, M. Fan, W.-P. Chen, Y. Yu, X. Liu, Q. Meng, S. Xin, Y.-X. Yin, Y.-G. Guo, *Nat. Commun.* **2021**, *12*, 5267.
- [32] Y. Li, Q. Liu, S. Wu, L. Geng, J. Popovic, Y. Li, Z. Chen, H. Wang, Y. Wang, T. Dai, Y. Yang, H. Sun, Y. Lu, L. Zhang, Y. Tang, R. Xiao, H. Li, L. Chen, J. Maier, J. Huang, Y.-S. Hu, *J. Am. Chem. Soc.* **2023**, *145*, 10576–10583.
- [33] S. Chu, C. Zhang, H. Xu, S. Guo, P. Wang, H. Zhou, *Angew. Chem. Int. Ed.* **2021**, *60*, 13366–13371.
- [34] X. Cui, S. Wang, X. Ye, X. Fan, C. Gao, Y. Quan, S. Wen, X. Cai, J. Huang, S. Li, *Energy Storage Mater.* **2022**, *45*, 1153–1164.
- [35] F. Wang, B. Peng, S. Zeng, L. Zhao, X. Zhang, G. Wan, H. Zhang, G. Zhang, *Adv. Funct. Mater.* **2022**, *32*, 2202665.
- [36] X. Yuan, Y. Guo, L. Gan, X. Yang, W. He, X. Zhang, Y. Yin, S. Xin, H. Yao, Z. Huang, Y. Guo, *Adv. Funct. Mater.* **2022**, *32*, 2111466.
- [37] J. Yang, J. Lim, M. Park, G. Lee, S. Lee, M. Cho, Y. Kang, *Adv. Energy Mater.* **2021**, *11*, 2102444.
- [38] C. Zhao, Z. Yao, Q. Wang, H. Li, J. Wang, M. Liu, S. Ganapathy, Y. Lu, J. Cabana, B. Li, X. Bai, A. Aspuru-Guzik, M. Wagemaker, L. Chen, Y.-S. Hu, *J. Am. Chem. Soc.* **2020**, *142*, 5742–5750.
- [39] L. Zhang, J. Wang, G. Schuck, F. Xi, L. Du, M. Winter, G. Schumacher, J. Li, *Small Methods* **2020**, *4*, 2000422.
- [40] S. Kang, D. Choi, H. Lee, B. Choi, Y.-M. Kang, *Adv. Mater.* **2023**, *35*, 2211965.
- [41] Y. Kobayashi, M. Sawamura, S. Kondo, M. Harada, Y. Noda, M. Nakayama, S. Kobayakawa, W. Zhao, A. Nakao, A. Yasui, H. B. Rajendra, K. Yamanaka, T. Ohta, N. Yabuuchi, *Mater. Today* **2020**, *37*, 43–55.
- [42] P. Wang, Y. Meng, Y. Wang, L. Chen, Z. Zhang, W. Pu, J. Li, C. Yang, D. Xiao, *Energy Storage Mater.* **2022**, *44*, 487–496.
- [43] J. Zhang, Q. Zhang, D. Wong, N. Zhang, G. Ren, L. Gu, C. Schulz, L. He, Y. Yu, X. Liu, *Nat. Commun.* **2021**, *12*, 3071.
- [44] M. Yoon, Y. Dong, J. Hwang, J. Sung, H. Cha, K. Ahn, Y. Huang, S. J. Kang, J. Li, J. Cho, *Nat. Energy* **2021**, *6*, 362–371.
- [45] B. Xiao, Y. Wang, S. Tan, M. Song, X. Li, Y. Zhang, F. Lin, K. S. Han, F. Omenya, K. Amine, X.-Q. Yang, D. Reed, Y. Hu, G.-L. Xu, E. Hu, X. Li, X. Li, *Angew. Chem. Int. Ed.* **2021**, *60*, 8258–8267.
- [46] Q. Shen, Y. Liu, X. Zhao, J. Jin, Y. Wang, S. Li, P. Li, X. Qu, L. Jiao, *Adv. Funct. Mater.* **2021**, *31*, 2106923.

- [47] B. Mortemard De Boisse, G. Liu, J. Ma, S. Nishimura, S.-C. Chung, H. Kiuchi, Y. Harada, J. Kikkawa, Y. Kobayashi, M. Okubo, A. Yamada, *Nat. Commun.* **2016**, *7*, 11397.
- [48] A. J. Perez, D. Batuk, M. Saubanère, G. Rousse, D. Foix, E. McCalla, E. J. Berg, R. Dugas, K. H. W. van den Bos, M.-L. Doublet, D. Gonbeau, A. M. Abakumov, G. Van Tendeloo, J.-M. Tarascon, *Chem. Mater.* **2016**, *28*, 8278–8288.
- [49] R. A. House, U. Maitra, L. Jin, J. G. Lozano, J. W. Somerville, N. H. Rees, A. J. Naylor, L. C. Duda, F. Massel, A. V. Chadwick, S. Ramos, D. M. Pickup, D. E. McNally, X. Lu, T. Schmitt, M. R. Roberts, P. G. Bruce, *Chem. Mater.* **2019**, *31*, 3293–3300.
- [50] Y. Xie, E. Gabriel, L. Fan, I. Hwang, X. Li, H. Zhu, Y. Ren, C. Sun, J. Pipkin, M. Dustin, M. Li, Z. Chen, E. Lee, H. Xiong, *Chem. Mater.* **2021**, *33*, 4445–4455.
- [51] J. Xu, D. H. Lee, R. J. Clément, X. Yu, M. Leskes, A. J. Pell, G. Pintacuda, X.-Q. Yang, C. P. Grey, Y. S. Meng, *Chem. Mater.* **2014**, *26*, 1260–1269.
- [52] X. Rong, J. Liu, E. Hu, Y. Liu, Y. Wang, J. Wu, X. Yu, K. Page, Y.-S. Hu, W. Yang, H. Li, X.-Q. Yang, L. Chen, X. Huang, *Joule* **2018**, *2*, 125–140.
- [53] N. Yabuuchi, R. Hara, M. Kajiyama, K. Kubota, T. Ishigaki, A. Hoshikawa, S. Komaba, *Adv. Energy Mater.* **2014**, *4*, 1301453.
- [54] K. Du, J. Zhu, G. Hu, H. Gao, Y. Li, J. B. Goodenough, *Energy Environ. Sci.* **2016**, *9*, 2575–2577.
- [55] X. Rong, E. Hu, Y. Lu, F. Meng, C. Zhao, X. Wang, Q. Zhang, X. Yu, L. Gu, Y.-S. Hu, H. Li, X. Huang, X.-Q. Yang, C. Delmas, L. Chen, *Joule* **2019**, *3*, 503–517.
- [56] C. Cai, X. Li, P. Hu, T. Zhu, J. Li, H. Fan, R. Yu, T. Zhang, S. Lee, L. Zhou, L. Mai, *Adv. Funct. Mater.* **2023**, *33*, 2215155.
- [57] Z. Wu, Y. Ni, S. Tan, E. Hu, L. He, J. Liu, M. Hou, P. Jiao, K. Zhang, F. Cheng, J. Chen, *J. Am. Chem. Soc.* **2023**, *145*, 9596–9606.
- [58] Z. Chen, M. Yang, G. Chen, G. Tang, Z. Huang, M. Chu, R. Qi, S. Li, R. Wang, C. Wang, T. Zhang, J. Zhai, W. Zhao, J. Zhang, J. Chen, L. He, J. Xu, W. Yin, J. Wang, Y. Xiao, *Nano Energy* **2022**, *94*, 106958.
- [59] B. Mortemard de Boisse, S. Nishimura, E. Watanabe, L. Lander, A. Tsuchimoto, J. Kikkawa, E. Kobayashi, D. Asakura, M. Okubo, A. Yamada, *Adv. Energy Mater.* **2018**, *8*, 1800409.
- [60] X. Li, T. Wang, Y. Yuan, X. Yue, Q. Wang, J. Wang, J. Zhong, R. Lin, Y. Yao, X. Wu, X. Yu, Z. Fu, Y. Xia, X. Yang, T. Liu, K. Amine, Z. Shadik, Y. Zhou, J. Lu, *Adv. Mater.* **2021**, *33*, 2008194.
- [61] S. Komaba, N. Yabuuchi, T. Nakayama, A. Ogata, T. Ishikawa, I. Nakai, *Inorg. Chem.* **2012**, *51*, 6211–6220.
- [62] P.-F. Wang, H.-R. Yao, X.-Y. Liu, J.-N. Zhang, L. Gu, X.-Q. Yu, Y.-X. Yin, Y.-G. Guo, *Adv. Mater.* **2017**, *29*, 1700210.
- [63] Q. Liu, Z. Hu, M. Chen, C. Zou, H. Jin, S. Wang, Q. Gu, S. Chou, *J. Mater. Chem. A* **2019**, *7*, 9215–9221.
- [64] R. J. Clément, P. G. Bruce, C. P. Grey, *J. Electrochem. Soc.* **2015**, *162*, A2589.
- [65] Y. Zhu, Y. Xiao, W. Hua, S. Indris, S. Dou, Y. Guo, S. Chou, *Angew. Chem. Int. Ed.* **2020**, *59*, 9299–9304.
- [66] R. Berthelot, D. Carlier, C. Delmas, *Nat. Mater.* **2011**, *10*, 74–80.
- [67] M. Guignard, C. Didier, J. Darriet, P. Bordet, E. Elkaïm, C. Delmas, *Nat. Mater.* **2013**, *12*, 74–80.
- [68] Q. Pei, M. Lu, Z. Liu, D. Li, X. Rao, X. Liu, S. Zhong, *ACS Appl. Energ. Mater.* **2022**, *5*, 1953–1962.
- [69] Z. Xiao, W. Zuo, X. Liu, J. Xie, H. He, Y. Xiang, H. Liu, Y. Yang, *ACS Appl. Mater. Interfaces* **2021**, *13*, 38305–38314.
- [70] Y. Shi, P. Jiang, S. Wang, W. Chen, B. Wei, X. Lu, G. Qian, W. H. Kan, H. Chen, W. Yin, Y. Sun, X. Lu, *Nat. Commun.* **2022**, *13*, 7888.
- [71] P.-F. Wang, H.-R. Yao, X.-Y. Liu, Y.-X. Yin, J.-N. Zhang, Y. Wen, X. Yu, L. Gu, Y.-G. Guo, *Sci. Adv.* **2018**, *4*, 6018–6027.
- [72] Q. Wang, Z. Shadik, X. Li, J. Bao, Q. Qiu, E. Hu, S. Bak, X. Xiao, L. Ma, X. Wu, X. Yang, Y. Zhou, *Adv. Energy Mater.* **2021**, *11*, 2003455.
- [73] T. Jin, P.-F. Wang, Q.-C. Wang, K. Zhu, J. Zhang, W. Zhang, X.-Q. Yang, C. Wang, *Angew. Chem. Int. Ed.* **2020**, *59*, 14511–14516.
- [74] X. Wang, X. Dong, X. Feng, Q. Shi, J. Wang, X. Yin, J. Zhang, Y. Zhao, *Small Methods* **2023**, *7*, 2201201.
- [75] C. Cheng, H. Hu, C. Yuan, X. Xia, J. Mao, K. Dai, L. Zhang, *Energy Storage Mater.* **2022**, *52*, 10–18.
- [76] T. Zhang, H. Ji, X. Hou, W. Ji, H. Fang, Z. Huang, G. Chen, T. Yang, M. Chu, S. Xu, Z. Chen, C. Wang, W. Yang, J. Yang, X. Ma, K. Sun, D. Chen, M. Tao, Y. Yang, J. Zheng, F. Pan, Y. Xiao, *Nano Energy* **2022**, *100*, 107482.
- [77] W. Zuo, J. Qiu, X. Liu, F. Ren, H. Liu, H. He, C. Luo, J. Li, G. F. Ortiz, H. Duan, J. Liu, M.-S. Wang, Y. Li, R. Fu, Y. Yang, *Nat. Commun.* **2020**, *11*, 3544.
- [78] L. Zhengbo, X. Xijun, J. Shaomin, Z. Liyan, Z. Dechao, L. Jun, *Chem. Eur. J.* **2020**, *26*, 7747–7766.
- [79] Y.-F. Liu, K. Han, D.-N. Peng, L.-Y. Kong, Y. Su, H.-W. Li, H.-Y. Hu, J.-Y. Li, H.-R. Wang, Z.-Q. Fu, Q. Ma, Y.-F. Zhu, R.-R. Tang, S.-L. Chou, Y. Xiao, X.-W. Wu, *InfoMat* **2023**, *5*, e12422.
- [80] W. Shi, Y. Zheng, X. Meng, S. Liu, S. Xu, L. Chen, X. Wang, D. Zhang, *ChemElectroChem* **2020**, *7*, 2545–2552.
- [81] E. Oz, S. Altin, S. Avci, *ACS Omega* **2023**, *8*, 27170–27178.
- [82] R. Luo, J. Zheng, Z. Zhou, J. Li, Y. Li, Z. He, *ACS Appl. Mater. Interfaces* **2022**, *14*, 47863–47871.
- [83] W. Zuo, J. Qiu, X. Liu, B. Zheng, Y. Zhao, J. Li, H. He, K. Zhou, Z. Xiao, Q. Li, G. F. Ortiz, Y. Yang, *Energy Storage Mater.* **2020**, *26*, 503–512.
- [84] W. Zuo, X. Liu, J. Qiu, D. Zhang, Z. Xiao, J. Xie, F. Ren, J. Wang, Y. Li, G. F. Ortiz, W. Wen, S. Wu, M.-S. Wang, R. Fu, Y. Yang, *Nat. Commun.* **2021**, *12*, 4903.
- [85] C. Delmas, D. Carlier, M. Guignard, *Adv. Energy Mater.* **2021**, *11*, 2001201.
- [86] R. Zhang, S. Yang, H. Li, T. Zhai, H. Li, *InfoMat* **2022**, *4*, e12305.
- [87] J. Feng, C. Zheng, D. Fang, J. Li, *J. Energy Chem.* **2023**, *82*, 228–238.
- [88] L. Gan, X. Yuan, J. Han, X. Yang, L. Zheng, Z. Huang, H. Yao, *Adv. Funct. Mater.* **2023**, *33*, 2209026.
- [89] Y. Yu, D. Ning, Q. Li, A. Franz, L. Zheng, N. Zhang, G. Ren, G. Schumacher, X. Liu, *Energy Storage Mater.* **2021**, *38*, 130–140.
- [90] J. R. Joshua, Y. S. Lee, T. Maiyalagan, N. Nallamuthu, P. Yuvraj, N. Sivakumar, *Electroanal. Chem.* **2020**, *856*, 113633.
- [91] H. Li, S. Liu, H. Wang, B. Wang, P. Sheng, L. Xu, G. Zhao, H. Bai, X. Chen, Y. Cao, Z. Chen, *Acta Phys.-Chim. Sin.* **2019**, *35*, 1357–1364.
- [92] H. V. Ramasamy, K. Kaliyappan, R. Thangavel, V. Aravindan, K. Kang, D. U. Kim, Y. Park, X. Sun, Y.-S. Lee, *J. Mater. Chem. A* **2017**, *5*, 8408–8415.
- [93] H. G. Kim, Y. J. Park, *ACS Appl. Energ. Mater.* **2021**, *4*, 8220–8230.
- [94] X. Fan, C. Wang, *Chem. Soc. Rev.* **2021**, *50*, 10486–10566.
- [95] J. H. Jo, J. U. Choi, A. Konarov, H. Yashiro, S. Yuan, L. Shi, Y.-K. Sun, S.-T. Myung, *Adv. Funct. Mater.* **2018**, *28*, 1705968.
- [96] J.-N. Zhang, Q. Li, Y. Wang, J. Zheng, X. Yu, H. Li, *Energy Storage Mater.* **2018**, *14*, 1–7.
- [97] D. Bedrov, O. Borodin, J. B. Hooper, *J. Phys. Chem. C* **2017**, *121*, 16098–16109.
- [98] K. Xu, *Chem. Rev.* **2014**, *114*, 11503–11618.
- [99] J. Feng, D. Fang, Z. Yang, J. Zhong, C. Zheng, Z. Wei, J. Li, *J. Power Sources* **2023**, *553*, 232292.
- [100] Y. Yoda, K. Kubota, K. Kuroki, S. Suzuki, K. Yamanaka, T. Yaji, S. Amagasa, Y. Yamada, T. Ohta, S. Komaba, *Small* **2020**, *16*, 2006483.
- [101] T.-Y. Yu, J. Kim, J.-Y. Hwang, H. Kim, G. Han, H.-G. Jung, Y.-K. Sun, *J. Mater. Chem. A* **2020**, *8*, 13776–13786.
- [102] Y.-N. Zhou, P.-F. Wang, X.-D. Zhang, L.-B. Huang, W.-P. Wang, Y.-X. Yin, S. Xu, Y.-G. Guo, *ACS Appl. Mater. Interfaces* **2019**, *11*, 24184–24191.
- [103] L. Zheng, J. Li, M. N. Obrovac, *Chem. Mater.* **2017**, *29*, 1623–1631.
- [104] Z. Lu, R. A. Donaberger, J. R. Dahn, *Chem. Mater.* **2000**, *12*, 3583–3590.
- [105] Y. Hou, X. Li, W. Liu, H. Kou, H. Maleki Kheimeh Sari, X. Song, J. Li, S. Dou, X. Liu, S. Deng, D. Li, X. Sun, *Mater. Today Energy* **2019**, *14*, 100353.
- [106] A. Joshi, S. Chakraborty, S. H. Akella, A. Saha, A. Mukherjee, B. Schmerling, M. Ejgenberg, R. Sharma, M. Noked, *Adv. Mater.* **2023**, *33*, 2304440.
- [107] J. James Abraham, C. R. A. Arro, H. A. Tariq, R. Kahraman, S. Al-Qaradawi, T. M. Al tahtamouni, R. A. Shakoor, *J. Power Sources* **2021**, *506*, 230098.
- [108] Z. Liu, C. Zhou, J. Liu, L. Yang, J. Liu, M. Zhu, *Chem. Eng. J.* **2022**, *431*, 134273.
- [109] P. Zou, L. Yao, C. Wang, S. J. Lee, T. Li, H. L. Xin, *Angew. Chem. Int. Ed.* **2023**, *62*, e202304628.
- [110] X. Wang, X. Dong, X. Feng, X. Feng, Q. Shi, J. Wang, X. Yin, J. Zhang, Y. Zhao, *Small Methods* **2023**, *7*, 2201201.
- [111] J. Li, W. Zhong, Q. Deng, Q. Zhang, Z. Lin, C. Yang, *Adv. Funct. Mater.* **2023**, *33*, 2300127.
- [112] X. Li, Y. Wang, D. Wu, L. Liu, S.-H. Bo, G. Ceder, *Chem. Mater.* **2016**, *28*, 6575–6583.
- [113] L. Yang, Z. Liu, X. Shen, S. Li, Z. Hu, Q. Kong, J. Ma, J. Li, H.-J. Lin, C.-T. Chen, J.-M. Chen, S.-C. Haw, X. Wang, R. Yu, Z. Wang, L. Chen, *Energy Storage Mater.* **2022**, *44*, 231–238.
- [114] Y. Xiao, N. M. Abbasi, Y.-F. Zhu, S. Li, S.-J. Tan, W. Ling, L. Peng, T. Yang, L. Wang, X.-D. Guo, Y.-X. Yin, H. Zhang, Y.-G. Guo, *Adv. Funct. Mater.* **2020**, *30*, 2001334.

- [115] H. Zhang, Y. Gao, X. Liu, L. Zhou, J. Li, Y. Xiao, J. Peng, J. Wang, S.-L. Chou, *Adv. Energy Mater.* **2023**, *13*, 2300149.
- [116] H. Wu, J. Dong, Y. Zhang, L. Lin, G. Gao, T. Li, X. Yi, B. Sa, J. Wang, L. Wang, J. Li, K. Amine, D.-L. Peng, Q. Xie, *Adv. Funct. Mater.* **2023**, *33*, 2303707.
- [117] Y. Wang, Z. Shadike, W. Fitzhugh, F. Wu, S.-J. Lee, J.-S. Lee, X. Chen, Y. Long, E. Hu, X. Li, *Energy Storage Mater.* **2023**, *55*, 587–596.
- [118] K. Wang, W. Hua, X. Huang, D. Stenzel, J. Wang, Z. Ding, Y. Cui, Q. Wang, H. Ehrenberg, B. Breitung, C. Kübel, X. Mu, *Nat. Commun.* **2023**, *14*, 1487.
- [119] A. W. Tomich, J. Park, S.-B. Son, E. P. Kamphaus, X. Lyu, F. Dogan, V. Carta, J. Gim, T. Li, L. Cheng, E. Lee, V. Lavallo, C. S. Johnson, *Angew. Chem. Int. Ed.* **2022**, *61*, e202208158.
- [120] C. Luo, A. Langrock, X. Fan, Y. Liang, C. Wang, *J. Mater. Chem. A* **2017**, *5*, 18214–18220.
- [121] X. Luo, Q. Huang, Y. Feng, C. Zhang, C. Liang, L. Zhou, W. Wei, *ACS Appl. Mater. Interfaces* **2022**, *14*, 51846–51854.
- [122] H. Ji, J. Zhai, G. Chen, X. Qiu, H. Fang, T. Zhang, Z. Huang, W. Zhao, Z. Wang, M. Chu, R. Wang, C. Wang, R. Li, W. Zeng, X. Wang, Y. Xiao, *Adv. Funct. Mater.* **2022**, *32*, 2109319.
- [123] Q. Li, S. Xu, S. Guo, K. Jiang, X. Li, M. Jia, P. Wang, H. Zhou, *Adv. Mater.* **2020**, *32*, 1907936.
- [124] X. Liang, Y.-K. Sun, *Adv. Funct. Mater.* **2022**, *32*, 2206154.
- [125] W. Zuo, Y. Yang, *Acc. Mater. Res.* **2022**, *3*, 709–720.
- [126] F. Ding, C. Zhao, D. Zhou, Q. Meng, D. Xiao, Q. Zhang, Y. Niu, Y. Li, X. Rong, Y. Lu, L. Chen, Y.-S. Hu, *Energy Storage Mater.* **2020**, *30*, 420–430.
- [127] H. Ren, L. Zheng, Y. Li, Q. Ni, J. Qian, Y. Li, Q. Li, M. Liu, Y. Bai, S. Weng, X. Wang, F. Wu, C. Wu, *Nano Energy* **2022**, *103*, 107765.
- [128] Z. Cheng, B. Zhao, Y.-J. Guo, L. Yu, B. Yuan, W. Hua, Y.-X. Yin, S. Xu, B. Xiao, X. Han, P.-F. Wang, Y.-G. Guo, *Adv. Energy Mater.* **2022**, *12*, 2103461.
- [129] Y. Shi, Z. Zhang, P. Jiang, A. Gao, K. Li, Q. Zhang, Y. Sun, X. Lu, D. Cao, X. Lu, *Energy Storage Mater.* **2021**, *37*, 354–362.
- [130] R. Li, J. Gao, J. Li, H. Huang, X. Li, W. Wang, L. Zheng, S. Hao, J. Qiu, W. Zhou, *Adv. Funct. Mater.* **2022**, *32*, 2205661.
- [131] T. Song, C. Wang, L. Kang, W. Yao, H. Wang, H. Chen, Q. Liu, Y. Lu, Z. Guan, A. Zhu, T. Kang, Y. Tang, C.-S. Lee, *Adv. Energy Mater.* **2023**, *13*, 2302393.

Manuscript received: October 13, 2023

Revised manuscript received: December 30, 2023

Accepted manuscript online: January 5, 2024

Version of record online: January 17, 2024